Competitive Reaction of Neptunium(V) and Uranium(VI) in Potassium−Sodium Carbonate-Rich Aqueous Media: Speciation Study with a Focus on High-Resolution X-ray Spectroscopy

Tonya Vitova,*,[†] Ivan Pidchenko,[†] Dieter Schild,[†] Tim Prüßmann,[†] Vanessa Montoya,[†,§]
David Fellhauer,[†] Xavier Gaona,[†] Elke Bohnert,[†] Jörg Rothe, Robert J. Baker,*,[‡] and Horst Geckeis[†]

[†]Institute for Nuclear Waste Disposal (INE), Karlsruhe Institute of Technology, P.O. 3640, D 76021 Karlsruhe, Germany
[‡]School of Chemistry, University of Dublin, Trinity College, Dublin 2, Ireland

ABSTRACT: Neptunium(V) and uranium(VI) are precipitated from an aqueous potassium−sodium containing carbonate rich solution, and the solid phases are investigated. U/Np $M_{4,5}$ edge high energy resolution X ray absorption near edge structure (HR XANES) spectroscopy and Np 3d4f resonant inelastic X ray scattering (3d4f RIXS) are applied in combination with thermodynamic calculations, U/Np L_3 edge XANES, and extended X ray absorption fine structure (EXAFS) studies to analyze the local atomic coordination and oxidation states of uranium and neptunium. The XANES/HR XANES analyses are supported by ab initio quantum chemical computations with the finite difference method near edge structure code (FDMNES). The solid precipitates are also investigated with powder X ray diffraction, scanning electron microscopy−energy dispersive X ray spectros copy, and Raman spectroscopy. The results strongly suggest that $K[Np^{V}O_2CO_3]_{(cr)}$, $K_3[Np^{V}O_2(CO_3)_2]_{(cr)}$, and $K_3Na[U^{VI}O_2(CO_3)_3]_{(cr)}$ are the predominant neptunium and uranium solid phases formed. Despite the 100 times lower initial neptunium(V) concentration at pH 10.5 and oxic conditions, neptunium(V) rich phases predominately precipitate. The prevailing formation of neptunium(V) over uranium(VI) solids demonstrates the high structural stability of neptunium(V) carbonates containing potassium. It is illustrated that the Np M_5 edge HR XANES spectra are sensitive to changes of the Np−O axial bond length for neptunyl(V/VI).

INTRODUCTION

Neptunium 237 is an actinide with a long half life (2.14×10^6 years) and high specific activity presenting a complex redox and coordination chemistry in aqueous systems, which makes it difficult to study. For example, neptunium(V) carbonates have been investigated with a variety of spectroscopic techniques,[1] whereas a few examples of neptunium(VI) carbonates exist.[2] Only a few investigations exist regarding the interaction of Np with different minerals by adsorption or structural incorporation. Balboni et al. have shown that the incorporation of Np into carbonate minerals such as calcite ($CaCO_3$), aragonite ($CaCO_3$), and strontianite ($SrCO_3$) is possible.[3] Extended X ray absorption fine structure (EXAFS) was applied to study the speciation of Np coprecipitated with calcite[4] and sorbed[5] onto calcite. Studies dedicated to the interaction of Np with other minerals are even more scarce and focus mainly on Fe^{II} bearing minerals. When Np^{V} reacts with certain Fe^{II} phases, depending upon the conditions, reduction to Np^{IV} [6] and either sorption or precipitation have been observed.[7]

Depending on the geochemical conditions of the environ ment, different uranium (U) alteration products are expected.[8] For example, within the weathered U ore minerals, the mixed $U^{VI/V}$ oxidation state mineral wyartite ($CaU^{V}[(UO_2)_2(CO_3)O_4(OH)]\cdot 7H_2O$) can be formed after oxidation of uraninite (UO_2). This mineral can potentially incorporate minor pentavalent actinides (An) like Np^{V} and plutonium (Pu^{V}).[9] On the other hand, different U minerals were used in the literature to study the reactivity of Np with them, observing that ^{237}Np was sorbed onto their surface or pure Np solid phases were formed. It was also found that Np can be incorporated into the mineral structure by cation exchange or by substitution of a U^{VI} for a Np^{V} or Np^{VI} ion in the mineral framework, with or without a compensating charge balancing cation substitution.[10] Within the available experimental data, it seems that the structure and/or chemical composition of the U mineral phase is of direct importance to the amount of incorporated Np.[11] In this sense, several laboratory studies have already illustrated that the U alteration products can effectively retain Np by sorption or incorporation processes but then subsequently release it into the aqueous solution.[10]

In this work, we investigate the reactivity of U^{VI} and Np^V in a competitive reaction with a high content of carbonate and the presence of potassium (K) and sodium (Na) in the aqueous solution. The focus of our study is on speciation of the products formed by coprecipitation reactions of Np^V during synthesis of the uranium(VI) carbonate phase grimselite $(K_3Na[UO_2(CO_3)_3]\cdot H_2O_{(cr)})$. We apply the Np 3d4f resonant inelastic X ray scattering (3d4f RIXS) and Np M_5 edge high energy resolution X ray absorption near edge structure (HR XANES) experimental techniques. These are used here for the first time for determination of the oxidation state of Np.[12] Their sensitivity to the U/Np=O axial bond length in actinyls is also discussed. An $M_{4,5}$ edge HR XANES gives a significant advantage[12a] over the widely applied conventional An L_3 edge XANES mode in studies related to the oxidation states and electronic structures of the An elements.[13] It is very sensitive to minor amounts of An oxidation states in mixtures and directly probes the An 5f unoccupied states, which are sensitive to changes in the chemical bonding. In addition to Np M_5 edge and U M_4 edge HR XANES/3d4f RIXS, we also applied powder X ray diffraction (pXRD), scanning electron microscopy–energy dispersive X ray spectroscopy (SEM–EDX), Raman spectroscopy, and U/Np L_3 edge XANES and EXAFS techniques as well as thermodynamic calculations. Computations of U/Np L_3 edge, Np M_5 edge, and U M_4 and M_5 edge HR XANES spectra were performed with the ab initio finite difference method near edge structure (FDMNES) code based on the multiple scattering theory.[23b] The combination of conventional and modern spectroscopic tools and thermodynamic calculations gives conclusive evidence for the Np and U oxidation states and coordination environment, thereby providing knowledge about the chemical behavior of Np^V when precipitated with higher amounts of U^{VI} in a $K-Na-CO_3-H_2O$ system.

MATERIAL AND METHODS

Caution! ^{237}Np *is a radioactive isotope and an α emitter. It should be handled in dedicated facilities with the appropriate equipment for radioactive materials to avoid health risks caused by radiation exposure.*

Synthesis. A grimselite $(K_3Na[UO_2(CO_3)_3]\cdot H_2O_{(cr)})$ reference sample was synthesized according to the procedure reported in the literature.[14] A Np stock solution was prepared from 16.2 mg of a $^{237}Np^V$ aqua complex dissolved in 0.055 M $HClO_4$ to give a total volume of 9.86 mL. The $[Np] = 6.9 \times 10^{-3}$ M concentration was determined by liquid scintillation counting. Under ambient conditions, a vial was charged with $UO_2(NO_3)_2\cdot 6H_2O$ ($[U] = 9.9 \times 10^{-3}$ M; $[NO_3] = 1.8 \times 10^{-2}$ M), Na_2CO_3 ($[Na] = 0.24$ M), K_2CO_3 ($[K] = 0.74$ M), and $[CO_3]_{TOT} = 0.49$ M solutions and Milli Q water with 20 mL of total volume. A total of 0.246 mL of a Np^V stock solution was then added and the vial stoppered. The resulting $[U]$ and $[Np]$ in the aqueous solution were 9.9×10^{-3} and 8.4×10^{-5} M, respectively. The pH was about 10.5, and the conditions were oxic. After the solution was left standing for 2 weeks, a light green precipitate formed, which was isolated and quickly washed with water $(2 \times 1$ mL), and the samples were prepared for measurements. The following nomenclature is used: Np cp, Np in a Np(U) precipitate; U cp, U in a Np(U) precipitate; grimselite, $K_3Na[UO_2(CO_3)_3]_{(cr)}$; metaschoepite, $UO_3\cdot nH_2O$ ($n < 2$) used as a reference, prepared via the literature procedure, and confirmed by pXRD and vibrational spectroscopy.[15]

pXRD, SEM–EDX, and Raman Spectroscopy. The pXRD patterns for both grimselite and the Np(U) precipitate were collected using a Bruker AXS D8 powder diffractometer equipped with a Baltic Scientific Instrument silicon (lithium) solid detector and a Cu $K\alpha$ X ray source. The Np(U) precipitate was studied by SEM–EDX, applying a Quanta 650 FEG (FEI, The Netherlands) equipped with a silicon drift X ray detector (Thermo Scientific, model UltraDry). The Raman spectra were measured at room temperature using a Bruker Senterra dispersive Raman microscope at 532 nm excitation wavelength; a few small crystals of the Np(U) precipitate were placed into a 1 mL glass vial and dried onto the inner wall surface.

X-ray Absorption Spectroscopy (XAS). The U/Np L_3 edge EXAFS and Np/U $M_{4,5}$ edge HR XANES/3d4f RIXS measurements were performed at the INE Beamline, Karlsruhe Research Accelerator (KARA), Karlsruhe, Germany.[16] Two Ge(422) and two Si(111) crystals were mounted in the double crystal monochromator (DCM) for An L_3 or $M_{4,5}$ edge XAS measurements, respectively. The beam was focused to ~0.5 mm vertically and ~0.5 mm horizontally onto the sample. For the U/Np $M_{4,5}$ edge HR XANES experiments, the Np(U) precipitate was placed into a double containment aluminum cell, where the inner compartment was sealed by 8 μm and the outer compartment by 13 μm Kapton foil, respectively (Figure S1). The grimselite and metaschoepite references were mixed with cellulose and pressed as pellets. Np M_5 and U M_4 edge XANES spectra were measured in high energy resolution mode (HR XANES) using an X ray emission multianalyzer crystal spectrometer (MAC Spectrometer).[17,18] The MAC Spectrometer was also applied for Np 3d4f RIXS measurements. The sample, five Si(220) analyzer crystals, and a detector (single diode silicon drift detector, SDD Vortex) were positioned on a Rowland circle in the vertical plane with a diameter of 1 m equal to the bending radius of the spherically bent analyzer crystals. The MAC Spectrometer was set at the maxima of the Np M_α (M_5N_7, $E = 3261.0$ eV) and U M_β (M_4N_6, $E = 3337.0$ eV) emission lines at 81.92° and 75.36° Bragg angles, respectively. The energies of the emission lines and the absorption edges are taken from the program *PyMca*[19] because the energies of the M_5N_7 and M_5N_6 emission lines are listed separately, in contrast to the program *Hephaestus*[20] previously used. A glovebox filled with helium and equipped with a lock chamber for transfer of the samples was built around the MAC Spectrometer to minimize loss of X ray intensity during the measurements in the tender X ray range of Np M_5 ($E = 3664$ eV) and U M_4 ($E = 3726$ eV) absorption edges. A constant helium flow was maintained; the dioxygen level was monitored continuously and kept constant (~0.1%) inside the glovebox. The experimental energy resolution during the Np M_5 edge HR XANES measurements was 1.0 eV, which was determined by measuring the full width at half maximum of the elastic peak at the 81.92° Bragg angle of the analyzer crystals. The DCM was calibrated by setting the energy position of the main absorption maximum (white line, WL) of the U M_4 edge HR XANES spectrum of a reference UO_2 sample to 3725.2 eV. Np/U M_5/M_4 edge HR XANES and normal emission spectra of $NpO_{2(am,hyd)}/UO_{2(cr)}$ were measured after each sample to verify the energy calibration of the DCM and the alignment of the MAC Spectrometer. No shifts of the normal emission lines measured for each sample were found during the experiments. For recording the Np 3d4f RIXS maps and the HR XANES spectra, the following parameters were applied: Np RIXS, excitation energy 3659–3684 eV, step size 0.5 eV, emission energy 3248–3268 eV, step size 0.25 eV, integration time 2 s; U M_4 and Np M_5 edge HR XANES, energy ranges are relative to the main absorption maximum: −15 to −5 eV, step size 0.5 eV, −5 to +15 eV, step size 0.1 eV, +15 to + 65 eV, step size 0.5 eV, integration time 1 s. The INE Beamline is a bending magnet beamline with $<10^9$ ph/s onto the sample at 3–4 keV. We first measured Np^{VI} in an aqueous solution, which is much more sensitive to radiation damage; we did not observe any damage for this liquid material. We measured several spectra for each of the Np and U solid samples and did not observe any changes.

For the U and Np L_3 edge EXAFS measurements of the Np(U) precipitate, a sample aliquot was placed into 300 μL Eppendorf vials in air. The oscillating $\chi(k)$ (EXAFS) part of the X ray absorption fine structure (XAFS) spectrum was extracted, Fourier transformed (FT), and modeled by using the *ATHENA* and *ARTEMIS* programs, respectively, parts of the *IFFEFIT* program package.[20] The $\chi(k)$

Table 1. EXAFS Fit Results for Np cp, U cp, and Grimselite[a]

sample	SP		N	R (Å)	$\sigma^2 \times 10^{-3}$ (Å^2)	ΔE_0 (eV)	r (%)
Np-cp [Np in Np(U) precipitate]	Np	O1	2[f]	1.83(1)	0.8(7)	7.4(11)	0.5
	Np	O2	5.4(4)	2.53(1)	6(1)		
	Np	C	2.9(10)	2.99(4)	6(1)		
U-cp [U in Np(U) precipitate]	U	O1	2.4[f]	1.78(1)	1.0(9)	4.3(4)	0.4
	U	O2	5.9(5)	2.44(1)	4(1)		
	U	C	3.5(4)	2.91(2)	4(1)		
	U	K	5.0(18)	4.02(2)	8(3)		
grimselite (reference)	U	O1	2[f]	1.80(1)	2(1)	3.2(8)	0.7
	U	O2	5.3(5)	2.41(1)	6(1)		
	U	C	2.7(7)	2.90(2)	6(1)		
	U	K	5.1 ± 1.9	3.98(3)	7(2)		

[a]SP = scattering path, N = coordination number, R = interatomic distance, σ^2 = DW factor, ΔE_0 = energy shift of the ionization potential, and r = goodness of fit parameter. The S_0^2 amplitude reduction factor is fixed to 0.8. Uncertainties are given in parentheses as the last decimal in the fit value. [f]Parameters are fixed. The O coordination number in the Np−O1 scattering path was first fixed to 2. As a second step, N and R were consecutively varied until the best fit was obtained.

spectra within the 2.6−10.4 Å^{-1} range for Np cp, 2.6−8.6 Å^{-1} for U cp, and 2.6−10.6 Å^{-1} for grimselite were weighted by k = 1, 2, or 3, and Hanning windows with sills equal to 2 (dk = 2) were applied. The fits were performed in R space for the 1.0−3.0 Å range (Np cp) and for 1.0−4.1 Å (U cp and grimselite). Three shells were modeled for Np (two Np−O and one Np−C distances) and four shells for U (two U−O, one U−C, and one U−K distances). The structures of K$_3$[NpO$_2$(CO$_3$)$_2$]·nH$_2$O$_{(cr)}$ (reproduced from Volkov et al.[21]) and grimselite mineral K$_3$Na[(UO$_2$)(CO$_3$)$_3$]·H$_2$O$_{(cr)}$ (AMCSD 0005731) were used as the initial models for the fit of the Np and U EXAFS spectra, respectively. The FEFF input files were generated by the FEFF9.6 ab initio quantum chemical theoretical code based on the multiple scattering theory.[22] The scattering potentials were calculated for a cluster of 59 atoms by including the self consistent field loop (SCF4.0). The amplitude reduction factor (S_0^2) was set to 0.8 for Np and U, which is an average value as determined for previous EXAFS measurements performed in the fluorescence mode at the INE Beamline. The shells of the Np FT EXAFS spectrum were fit in the order Np−O1, Np−O2, and Np−C, and those for U FT EXAFS in the order U−O1, U−O2, U−C, and U−K. For each shell, initially the interatomic distances (R) were varied, while the coordination numbers (N) were fixed; N and R were consecutively varied until the best fit was obtained; this procedure was repeated for each shell. The Debye−Waller (DW) factors and energy shifts of the ionization potential (ΔE_0) were always varied. The number of variables was kept approximately half the number of independent data points during the fitting procedure. A goodness of fit parameter (r) within 0.004−0.007, which is a 0.4−0.7% difference between the data and model, was obtained for the fits. The ΔE_0 parameters were found around 7.4(1) for Np cp, 4.3(4) for U cp, and 3.2(8) for grimselite (for details, see Table 1).

Computations of U and Np L$_3$-Edge XANES and M$_{4,5}$-Edge HR-XANES Spectra. U and Np L$_3$ edge XANES and M$_{4,5}$ edge HR XANES as well as DOS spectra were computed with the FDMNES code.[23] These ab initio calculations were performed for a cluster with 6 Å radius (≈60 atoms, L$_3$ edge)/3.5 Å radius (M$_{4,5}$ edge) using Green's function formalism, muffin tin potentials (L$_3$), or the finite difference method (M$_{4,5}$) and taking into account spin−orbit interactions. The Fermi energy was determined using self consistent field calculations. The calculation approach described by Vitova et al.[12g] was used for calculations of the M$_{4,5}$ edge spectra. The calculated U M$_4$ and Np M$_5$ edge HR XANES spectra with and without quadrupole transitions are identical. The calculated L$_3$ edge spectra were convoluted using the default values of FDMNES, and experimental broadening was not included. The convolution parameters for the M$_{4,5}$ edge HR XANES spectra are given in the Supporting Information (SI). Examples of the input files are also provided in the SI. The U L$_3$ edge spectra were calculated for the following crystal structures: K$_3$Na[UO$_2$(CO$_3$)$_3$]·H$_2$O$_{(cr)}$ (grimselite,

ICSD 186867; Figure S4 depicts the grimselite spectrum calculated using AMCSD 0005731, which is very similar) and UO$_2$CO$_3$·H$_2$O (rutherfordine, ICSD 87760). The Np L$_3$ edge spectra for K[NpO$_2$CO$_3$]$_{(cr)}$ (ICSD 15685; Pu is exchanged with Np; lattice parameters $a = b$ = 5.09 Å and c = 9.83 Å) and K$_3$[NpO$_2$(CO$_3$)$_2$]$_{(cr)}$ (reproduced from Volkov et al.[21]) were calculated. We verified this approach by applying the same crystal structure (grimselite with either U or Np) and found that the spectra are very similar, as can be expected for a $Z \pm 1$ difference (Figure S5). For calculation of the Np L$_3$ edge XANES of K[NpO$_2$CO$_3$]$_{(cr)}$, the lattice parameters $a = b$ = 5.12 Å and c = 9.971 Å reported by Keenan and Kruse[24] were also applied; the spectrum is similar to that calculated for ICSD 15685 and exchanging Pu with Np (Figure S6). We verified the influence of the cluster size on the spectra by increasing the size of the atomic cluster to 7 Å for grimselite (94 atoms) and rutherfordine (100 atoms). The computed spectra do not considerably differ (not shown). U M$_4$ and M$_5$ edge HR XANES and DOS spectra were calculated for grimselite. Np M$_5$ edge HR XANES and DOS were calculated for K[NpO$_2$CO$_3$]$_{(cr)}$ and K$_3$[NpO$_2$(CO$_3$)$_2$]$_{(cr)}$. In both cases, the same structures as those for the L$_3$ edge calculations were used.

Thermodynamic Calculations. Calculations were performed at 25 °C with the PHREEQC 3.3 code.[25] The activity coefficient formalism of Specific Interaction Theory (SIT) was used to describe the deviations from ideal chemical behavior that occur in concentrated electrolyte media. The ThermoChimie v9.b database was selected as the primary database because it provides an internally consistent database with SIT interaction coefficients capable of reproducing measured and observed behaviors of the Np and U systems.[26] Additionally, thermodynamic data for the potassium neptunium(V) carbonate solids, grimselite (K$_3$Na[(UO$_2$)(CO$_3$)$_3$]·H$_2$O$_{(cr)}$), and SIT coefficients for anions with K$^+$ were included from ref 27. However, considering the uncertainties in the thermodynamic data selection of grimselite, the solubility constant of this solid must be considered to be only provisional in thermodynamic calculations.

RESULTS

The synthesis of grimselite (K$_3$Na[UO$_2$(CO$_3$)$_3$]·H$_2$O$_{(cr)}$) with the addition of Np^V in the solution ([Np] = 8.4 × 10^{-5} M and [U] = 9.9 × 10^{-3} M) resulted in an intense green precipitate. In contrast, yellow crystals of grimselite were obtained in the absence of Np.[14] A significantly higher Np content compared to U in this precipitate was observed from SEM−EDX ([U] below the limit of detection; cf. the SEM−EDX results) and corroborated by Raman and X ray spectroscopies (vide infra). The intensity of the characteristic U M$_\beta$ fluorescence line was 4% of the Np M$_\alpha$ line (similar probability for emission) for the Np(U) precipitate, suggesting that the U concentration was
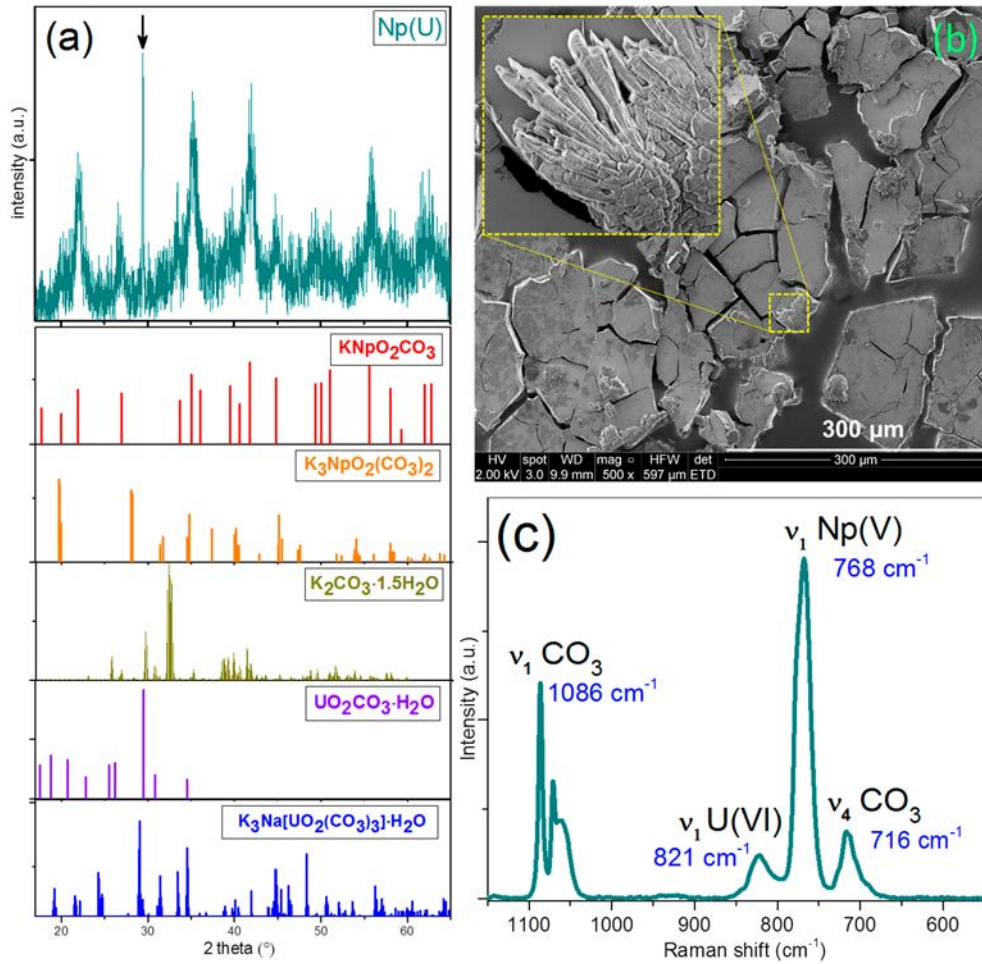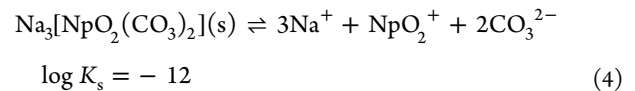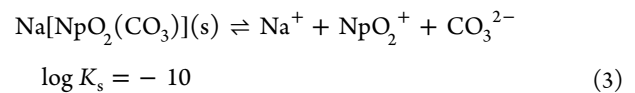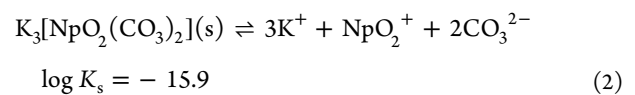
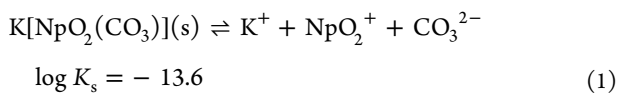**Figure 1.** (a) pXRD pattern of the Np(U) precipitate (top) with pXRD patterns (bottom) of $K[NpO_2CO_3]_{(cr)}$ (Bruker PDF 170264 based on ref 32a), $K_3[NpO_2(CO_3)_2]_{(cr)}$ (reproduced from Volkov et al.),[21] $K_2CO_3 \cdot 1.5H_2O$ (ISCD 22257), rutherfordine ($UO_2CO_3 \cdot H_2O_{(cr)}$; reproduced from Finch et al.),[34] and grimselite ($K_3Na[UO_2(CO_3)_3] \cdot H_2O_{(cr)}$, as measured with Bruker AXS D8; it agrees with AMCSD 0005731). The peak from possibly the U phase is indicated by a black arrow. (b) SEM images of the Np(U) precipitate and K_2CO_3 crystals formed on a cracked Np(U) precipitate after drying and preparation for SEM analysis (K_2CO_3 crystals are identified by the zoomed in regions). (c) Raman spectrum of the Np(U) precipitate.

about 4% of the Np concentration in the sample. This strong evidence for preferential Np phase precipitation over a U phase may be explained simply by differing solubility of neptunium(V)[28] and uranium(VI) carbonates for the given experimental conditions ([K] = 0.74 M, $[CO_3]_{TOT}$ = 0.49 M, pH ~10.5, and oxic conditions). Additionally, it is well known that K solid phases of Np^V can precipitate in alkaline solutions containing large Na and K concentrations, even if the concentration of Na^+ is much higher than that of K^+, which is supported by the difference of almost 4 orders of magnitude of the solubility constants of the solids containing K compared to their Na homologues (eqs 1–4).[29,30] The preferential precipitation could also be related to the formation of a metastable solid phase of Np, as described in the literature.[31] The green precipitate was analyzed by multiple techniques to identify its composition, U and Np local coordination environments, and oxidation states.

$$K[NpO_2(CO_3)](s) \rightleftharpoons K^+ + NpO_2^+ + CO_3^{2-}$$

$$\log K_s = -13.6 \tag{1}$$

$$K_3[NpO_2(CO_3)_2](s) \rightleftharpoons 3K^+ + NpO_2^+ + 2CO_3^{2-}$$

$$\log K_s = -15.9 \tag{2}$$

$$Na[NpO_2(CO_3)](s) \rightleftharpoons Na^+ + NpO_2^+ + CO_3^{2-}$$

$$\log K_s = -10 \tag{3}$$

$$Na_3[NpO_2(CO_3)_2](s) \rightleftharpoons 3Na^+ + NpO_2^+ + 2CO_3^{2-}$$

$$\log K_s = -12 \tag{4}$$

SEM−EDX. Traces of the crystalline K_2CO_3 phase are identified by SEM−EDX formed on the $Np^V(U)$ precipitate (Figures 1b and S2a−d). With SEM−EDX, it is difficult to detect characteristic X ray lines of U at low concentration beside intense Np lines because of their strong overlap. This is also valid for a small amount of Na in a sample with a high K content. The U concentration is estimated to be less than 10% of the Np concentration. Similarly, the Na concentration is estimated to be less than 10% of the K concentration in the Np(U) precipitate. At high magnification (100K×), a granular structure is observed by SEM, suggesting a particle size of

roughly 50 nm. Because the volume of the characteristic X rays generated at 30 kV of the primary electron beam is much larger than 50 nm, individual particle compositions of the Np(U) precipitate cannot be distinguished by SEM−EDX.

pXRD and Thermodynamic Calculations. The pXRD pattern of the Np(U) precipitate has main diffraction peaks similar to those found for $K[NpO_2CO_3]_{(cr)}$ reported by Keenan et al. and Visyashcheva et al. (Figure 1a).[32] However, the presence of $K_3[NpO_2(CO_3)_2]_{(cr)}$ cannot be excluded. $K[NpO_2CO_3]_{(cr)}$ is reported to form by adding K_2CO_3 to Np^V (10^{-5}–10^{-7} M) dilute acid solutions, obtaining a final carbonate concentration of <0.2 M, whereas $K_3[NpO_2(CO_3)_2]_{(cr)}$ is preferably formed in more concentrated K_2CO_3 solutions (∼0.5–2.0 M).[32,33] For 0.2–0.5 M K_2CO_3 solutions (this study), a metastable K–Np^V–CO_3 system is formed, where, depending on the conditions, either a $K[NpO_2CO_3]_{(cr)}$ or $K_3[NpO_2(CO_3)_2]_{(cr)}$ phase precipitates or they even coexist.[33] According to thermodynamic calculations, $K_3[NpO_2(CO_3)_2]_{(cr)}$ is predicted to be formed under the conditions selected for the present study (Pourbaix diagram in Figure 2b); however, it should be kept in mind that large uncertainties are expected in these simulations because of the combination of the high ionic strength of the system (i.e., ∼1 M), the presence of highly charged species in the aqueous solution (i.e., $NpO_2(CO_3)_3^{5-}$), and some unknown SIT coefficients in the thermodynamic database. The $K[NpO_2CO_3]_{(cr)}$ and $K_3[NpO_2(CO_3)_2]_{(cr)}$ phases have distinct structural differences but a similar design of the anionic layers $[NpO_2(CO_3)_x]^{(-2x+1)}$ (x = 1 or 2; Figure 3); in both compounds, the NpO_2^+ ion is coordinated by six O atoms originating from three carbonate ligands in the equatorial plane. The $K[NpO_2CO_3]_{(cr)}$ phase forms a hexagonal structure consisting of $[NpO_2CO_3]^-$ anionic layers with K^+ ions located between the layers. The $K_3[NpO_2(CO_3)_2]_{(cr)}$ phase has an orthorhombic structure where half of the NpO_2^+ moieties are replaced by K^+ ions. The $[NpO_2(CO_3)_2]^{3-}$ anionic layers are located at $^1/_2c$ crystallographic intervals and polymerize such that {−K−O=Np=O−K−O=Np=O−K−} infinite chains are formed along the c axis, with the closest Np−K atoms being found in the adjacent anionic layers.[21] Depending on the structure of the K–NpO_2–CO_3 phase, 0.5–2.0 H_2O molecules were reported to enter the structure, which are randomly distributed about the 4 fold positions between the anionic layers, likely enhancing the stability of the compound.[21] In the $M[NpO_2CO_3]_{(cr)}$ structures (M = Li, Na, K), the bond distance parameters vary depending on the alkaline metal, which defines the structural variations with an orthorhombic to hexagonal transformation on the Na−K boundary.[33b]

In Figure 1a, the most intense and narrow pXRD peak detected at $2\theta \approx 29°$ (highlighted with a black arrow) can be assigned to one of the uranyl carbonate phases, either rutherfordine ($[UO_2CO_3 \cdot H_2O_{(cr)}]$) or grimselite ($K_3Na[(UO_2)(CO_3)_3] \cdot H_2O_{(cr)}$). The latter option is supported by thermodynamic calculations, albeit with considerable uncertainties in the simulation, and the same caveats as in the case of Np also apply (Pourbaix diagram in Figure 2a). The structure of grimselite is different from those of the potassium neptunyl carbonates described above because it consists of a typical uranyl tricarbonate cluster $[(UO_2)(CO_3)_3]^{3-}$ forming a hexagonal bipyramid interconnected through bonds to Na and K polyhedra via U=O···M$^+$ interactions,[14] while the

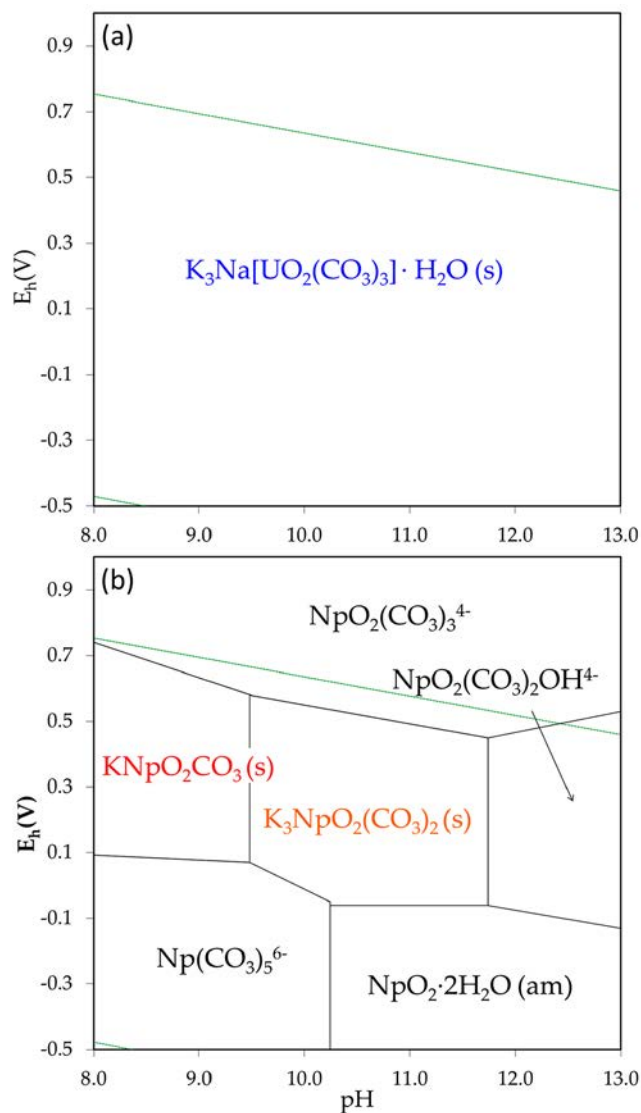**Figure 2.** (a) U and (b) Np Pourbaix diagrams: $[U]_{TOT}$ = 9.9×10^{-3} M, $[Np]_{TOT}$ = 8.4×10^{-5} M, Na_2CO_3 ([Na] = 0.24 M), K_2CO_3 ([K] = 0.74 M), $[CO_3]_{TOT}$ = 0.49 M. The expected phases are given in color.

structure of rutherfordine contains sheets of uranyl carbonate polyhedra (Figure 3).[34]

Raman Spectroscopy. Raman spectroscopy reveals bands for the Np(U) precipitate associated with the symmetric yl stretching: ν_1(Np=O) = 768 cm^{-1}; ν_1(U=O) = 821 cm^{-1} (Figure 1c). The Np=O stretch can be compared to that of $Na_3[NpO_2(CO_3)_2] \cdot nH_2O_{(cr)}$ [ν_1(Np=O) = 772 cm^{-1}][1d] because the spectrum for $M[NpO_2CO_3]_{(cr)}$ is not reported in the literature, while the uranyl stretch is similar to that in grimselite [ν_1(U=O) = 815 cm^{-1}][35] or in $UO_2CO_3 \cdot H_2O_{(cr)}$ [ν_1(U=O) = 837 cm^{-1}].[36] The Raman spectra also exhibit bands typical for the asymmetric deformation: ν_4 of the carbonate ion at 716 cm^{-1} and three bands at 1060, 1070, and 1086 cm^{-1} corresponding to the ν_1 symmetric stretch.

U and Np L$_3$-Edge EXAFS. To gain further insight into the local atomic environments of Np and U, we conducted an L$_3$ edge EXAFS spectroscopic study of Np and U in the Np(U) precipitate (Np cp and U cp). Grimselite ($K_3Na[(UO_2)(CO_3)_3] \cdot H_2O_{(cr)}$) was also investigated as a suitable U
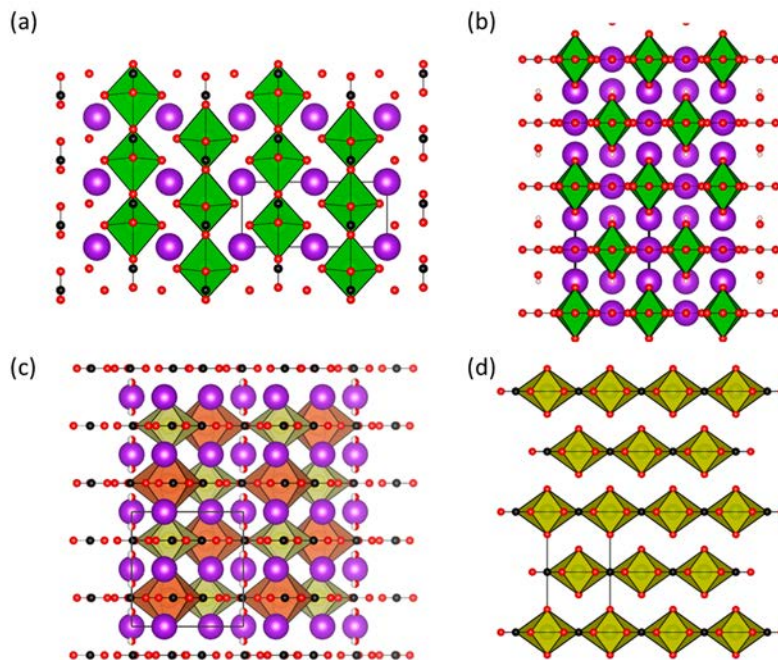
Figure 3. Structures of (a) K[NpO$_2$CO$_3$]$_{(cr)}$, (b) K$_3$[NpO$_2$(CO$_3$)$_2$]$_{(cr)}$, (c) grimselite (K$_3$Na[UO$_2$(CO$_3$)$_3$]·H$_2$O$_{(cr)}$), and (d) rutherfordine (UO$_2$CO$_3$·H$_2$O$_{(cr)}$) showing the different layer structures. Key: Np, green polyhedral; U, yellow polyhedral; Na, orange; K, purple; O, red; C, black.

reference. The Np and U L$_3$ edge FT EXAFS spectra and their best fits are depicted in Figure 4a–c. The Np FT EXAFS spectrum of Np cp reveals two intense peaks originating from scattering of the photoelectron from axial and equatorial O ligands (Figure 4a). The analyses result in two axial O atoms at an average distance (R) of R(Np–O$_{ax}$) = 1.83(1) Å from Np and in six equatorial O atoms at R(Np–O$_{eq}$) = 2.53(1) Å originating from three carbonates with R(Np–C) = 2.99(4) Å (Table 1). The EXAFS fits performed using three shells (O1 + O2 + C) or two shells (O1 + O2) showed that the data are better described with a three shell model (see Figure S3 and Table S1). The structure obtained from pXRD for K$_3$[NpO$_2$(CO$_3$)$_2$]·nH$_2$O$_{(cr)}$ exhibits the following average values for R(Np–O$_{ax}$) = 1.80 Å and R(Np–O$_{eq}$) = 2.58 [R(Np–C) is not reported].[21] The coordination of Np in K[NpO$_2$CO$_3$]$_{(cr)}$ has a more significant discrepancy for the axial bond R(Np–O$_{ax}$) = 1.96 Å, whereas the average equatorial R(Np–O$_{eq}$) = 2.57 Å bond and R(Np–C) = 2.96 Å are similar to the interatomic distances obtained for Np(U) (cf. Tables 1 and 2). No clear contribution from K atoms can be found in the EXAFS spectrum; K atoms are expected at ~3.8 Å (six atoms) for K[NpO$_2$CO$_3$]$_{(cr)}$.

In Table 1, the EXAFS best fit structural parameters for grimselite (K$_3$Na[(UO$_2$)(CO$_3$)$_3$]·H$_2$O$_{(cr)}$) are listed [R(U–O$_{ax}$) = 1.80(1) Å, R(U–O$_{eq}$) = 2.41(1) Å, and R(U–C) = 2.90(1) Å] and are close to those determined by X ray crystallography for grimselite [R(U–O$_{ax}$) = 1.78 Å, R(U–O$_{eq}$) = 2.42 Å, and R(U–C) = 2.89 Å].[14] The 0.08 Å elongation of R(U–K) found from the EXAFS fit [EXAFS, R(U–K) = 3.98(3) Å; pXRD, R(U–K) = 3.89 Å] might indicate structural disorder because EXAFS measures an average of the local coordination environments of all U atoms, whereas pXRD is sensitive only to the long range atomic order in the material.

The structural parameters for U cp slightly differ from those of grimselite (K$_3$Na[(UO$_2$)(CO$_3$)$_3$]·H$_2$O$_{(cr)}$); there is 0.02(1) and 0.03(1) Å shortening and elongation of the axial and
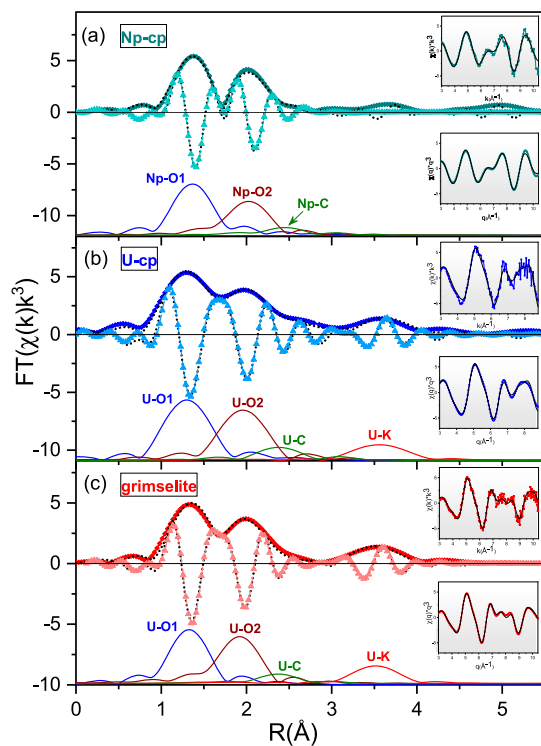

Figure 4. R space fit results for the (a) Np cp, (b) U cp, and grimselite (K$_3$Na[UO$_2$(CO$_3$)$_3$]·H$_2$O$_{(cr)}$) magnitudes of FT EXAFS (colored rhomboids) and their best fits (black dash dotted line) and single scattering paths, imaginary parts of FT EXAFS (light colored triangles) and their best fits (black dashed line) (top inset), k^3 weighted filtered $\chi(k)$ function (colored rhomboids) and their best fits (black solid line), and back transformed EXAFS and their back transformed fits (bottom inset).

equatorial U–O bonds, respectively [R(U–O$_{ax}$) = 1.78(1) Å and R(U–O$_{eq}$) = 2.44(1) Å; Tables 1 and 2]. This result

Table 2. U/Np−O and U/Np−C Interatomic Distances for the O and C Atoms in the First and Second Coordination Spheres of U and Np in Reference Solid Compounds proposed by XRD to Be Present in the Np(U) Precipitate

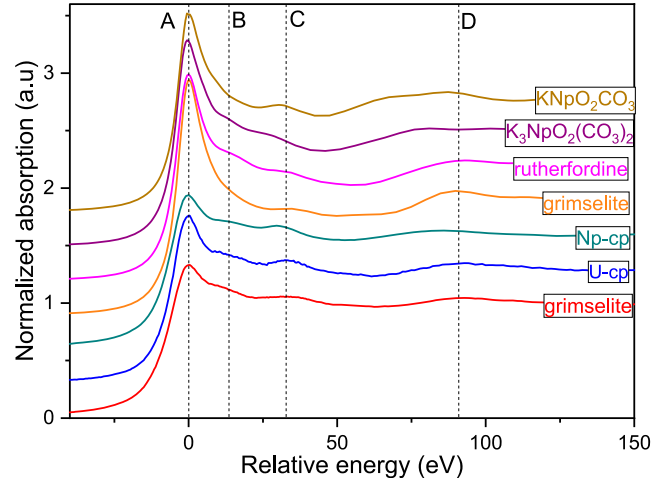| solid compound	$R(U-O_{ax})$ (Å)	$R(U-O_{eq})$ (Å)	$R(U-C)$ (Å)
K$_3$[NpO$_2$(CO$_3$)$_2$] nH$_2$O$_{(cr)}$ (Volkov et al.[21])	1.80	2.58	a
K[NpO$_2$CO$_3$]$_{(cr)}$ (ICSD 15685)	1.96	2.57	2.96
grimselite (K$_3$Na[UO$_2$(CO$_3$)$_3$] H$_2$O$_{(cr)}$; AMCSD 0005731)	1.78	2.42	2.89
rutherfordine (UO$_2$CO$_3$ H$_2$O$_{(cr)}$; ICSD 87760)	1.74	2.44 2.52	2.94

^{a}The U−C value is not reported in ref 21.

Figure 5. From bottom to top: experimental U L$_3$ edge XANES spectra of grimselite and U cp and Np L$_3$ edge XANES spectrum of Np cp. U L$_3$ edge XANES of grimselite (K$_3$Na[UO$_2$(CO$_3$)$_3$]·H$_2$O$_{(cr)}$) and rutherfordine (UO$_2$CO$_3$·H$_2$O$_{(cr)}$) and Np L$_3$ edge XANES of K$_3$[NpO$_2$(CO$_3$)$_2$]$_{(cr)}$ and K[NpO$_2$CO$_3$]$_{(cr)}$ computed with the FDMNES code. All spectra are aligned and plotted on a relative energy scale so that the most intense peak is at 0 eV.

agrees with the Raman spectroscopy and U M$_4$ edge HR XANES results (vide infra). Comparable U−C coordination numbers (N) and interatomic distances for U cp [$N = 3.1(8)$ and $R(U−C) = 2.91(2)$ Å] and grimselite [$N = 2.8(6)$ and $R(U−C) = 2.90(2)$ Å] are found (Table 1), suggesting the formation of similar uranyl tricarbonate compounds. The interatomic distances for rutherfordine (UO$_2$CO$_3$·H$_2$O$_{(cr)}$, ICSD 87760) deviate more substantially: $R(U−O_{ax}) = 1.74$ Å, $R(U−O_{eq}) = 2.44−2.52$ Å, and $R(U−C) = 2.94$ Å.

Both actinide elements are coordinated by carbonate, but interestingly the peak corresponding to K cannot be identified clearly in Np L$_3$ edge FT EXAFS, whereas it is well visible in both U L$_3$ edge FT EXAFS spectra, presumably because of the poor crystallinity of the Np solid phases (cf. Figure 4b,c).

No indication for coordination of U/Np with Np/U is found in the three FT EXAFS spectra because of very long $R(U/Np−Np/U)$ distance and/or disorder effects, e.g., $R(U−U) \sim 6.77$ Å for grimselite (K$_3$Na[(UO$_2$)(CO$_3$)$_3$]·H$_2$O$_{(cr)}$). Also, it must be remembered that EXAFS is usually not sensitive to Z differences of ±1.

U and Np L$_3$-Edge XANES. We compared experimental U and Np L$_3$ edge XANES spectra and corresponding spectra calculated with the FDMNES code. Those spectra fingerprint the local atomic environment of all U or Np atoms in the materials; therefore, the analyses are complementary to XRD and EXAFS. The U L$_3$ edge XANES experimental spectra for U cp and grimselite (Figure 5) are almost identical and very similar to the calculated U L$_3$ edge spectra of grimselite (K$_3$Na[(UO$_2$)(CO$_3$)$_3$]·H$_2$O$_{(cr)}$) and rutherfordine (UO$_2$CO$_3$·H$_2$O$_{(cr)}$). The energy positions of peaks C and D in the experimental Np L$_3$ edge XANES spectrum of Np cp are shifted to lower energies compared to the spectra of U cp and grimselite. Thus, the Np cp spectrum is more similar to the computed spectra of K[NpO$_2$CO$_3$]$_{(cr)}$ and K$_3$[NpO$_2$(CO$_3$)$_2$]· nH$_2$O$_{(cr)}$, in agreement with the EXAFS and XRD results. Note that the spectra are plotted on a relative energy scale and we did not find significant differences by calculating U or Np L$_3$ edge XANES for the same crystal structure (Figure S4). The main absorption peaks (WL) for the calculated spectra have much higher intensity because no experimental broadening is taken into account in the computations. The energy positions of the WLs of the U and Np L$_3$ edge XANES spectra correspond to oxidation states U^{VI} and Np^V. The spectra are compared to reference compounds in Figures S7 and S8.

Np 3d4f RIXS. To obtain further information on the oxidation state and coordination environment, we applied U M$_4$ edge HR XANES, Np 3d4f RIXS, and M$_5$ edge HR XANES spectroscopies.[12] Spectra for reference compounds

containing Np in its IV+, V+, and VI+ oxidation states were also recorded, namely, Np^{IV}O$_{2(am,hyd)}$, Ca$_{0.5}$Np^{V}O$_2$(OH)$_2$· 1.3H$_2$O$_{(cr)}$, and Na$_2$Np$^{VI}_2$O$_{7(cr)}$ (Figures 6 and 7).[37,38]

The Np 3d4f RIXS map is a two dimensional representation of the Np M$_\alpha$ emission line measured across the Np M$_5$ absorption edge.[12g] The Np M$_5$ edge HR XANES spectrum is a cross section of the RIXS map at a constant emission energy; i.e., the emission intensity integrated within the 0.1 eV emission energy range is plotted as a function of the excitation energy. Usually HR XANES is extracted at the maximum of the normal emission line measured at the excitation energy well above the main absorption peak (green line in Figure 6). However, we recently showed for U, Np, and Pu that the main resonant peak (the most intense structure in the RIXS maps) can be shifted to higher emission energies with respect to the normal emission line depending on the material (shift between the red and green lines in the RIXS maps in Figure 6). This shift was explained with variations of the interaction of the 3d excited electron in the 5f states and the created 4f core−hole and correlated with the level of localization of the 5f states.[12g] If the excited electron is in a more localized 5f state, the interaction will be stronger and the energy shift between the normal and resonant emissions will be larger. The energy shifts between the normal and resonant emissions for the Np^{IV}, Np^V, and Np^{VI} reference compounds are −1.0 ± 0.1 eV (Np^{IV} and Np^V) and 0.5 ± 0.1 eV (Np^{VI}) (Figure 6a−c). Accordingly, the 5f states are more delocalized for the Np^{VI} compound and similarly localized for the Np^{IV} and Np^V compounds. This energy shift is 0.7 ± 0.1 eV for Np 3d4f RIXS of the Np(U) precipitate (Figure 6d). Note that the oxidation state, and also the coordination environment and crystal structure, can influence the level of localization of the 5f states and thereby the magnitude of this energy shift. Because our references are oxides whereas the Np(U) solid is a carbonate material, a specific trend might not be observed; nevertheless, the energy shift for Np(U) is between the values found for Np^V and Np^{VI}. We recently observed that this energy shift in the An 3d4f RIXS maps also depends on the experimental energy resolution
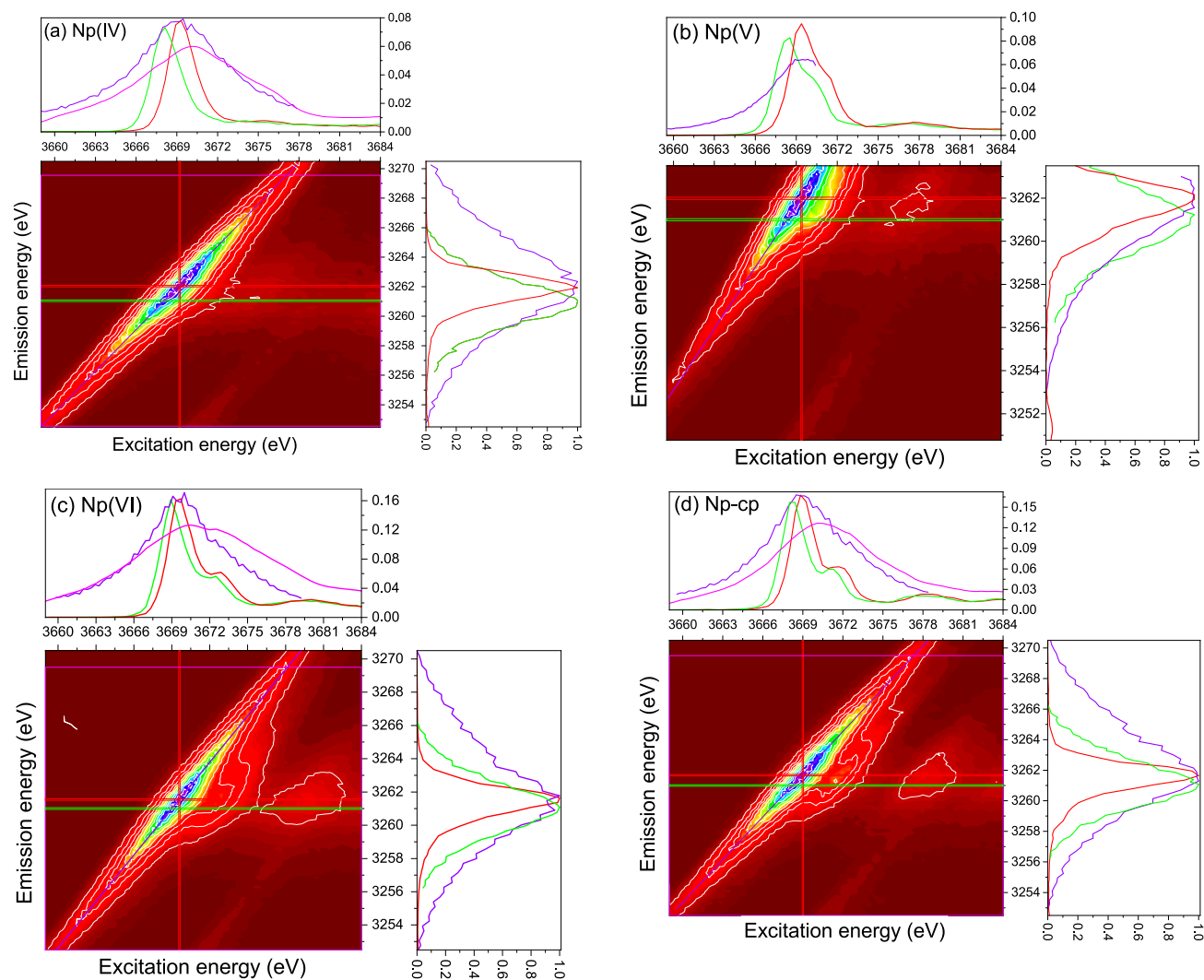
Figure 6. (a) Np 3d4f RIXS maps of $Np^{IV}O_{2(am,hyd)}$, (b) $Ca_{0.5}Np^{V}O_2(OH)_2·1.3H_2O_{(cr)}$, (c) $Na_2Np^{VI}_2O_{7(cr)}$, and (d) Np cp. The energy positions of the maxima of the normal (measured at 3700 eV excitation energy) and resonant emission lines are marked with horizontal green and red lines, respectively. Those lines are shown in green and red (obtained at the position of the red vertical line) on the right side of the maps. The violet line marks the cross section of the most intense resonance in the RIXS map. The cross sections plotted along the emission and the excitation energy scales are shown also with violet lines on the right and top of the RIXS maps, respectively. The rectangle in magenta with 17 eV width shows the emission energy region over which the intensity is integrated to obtain the conventional Np M_5 edge XANES spectrum plotted on the top also in magenta. The intensity of this spectrum is multiplied by 5.

(not shown); therefore, the RIXS maps should be measured at the same experimental conditions to allow for any comparison. We plotted the cross section of the main resonant peak along the emission and excitation energy axes (violet lines in Figure 6). It is clearly visible that the energy positions of the maxima of these cross sections, the resonant emission (red line on the right of the RIXS maps), and the main peak of HR XANES extracted at the maximum of the resonant peak agree well (red line on the top of the RIXS maps). In contrast, the HR XANES spectra extracted at the normal emission maxima and the normal emission lines are shifted to lower energy (green lines in Figure 6). The main absorption peak of these HR XANES spectra is a cross section of the tail of the broadening of the resonant peak; therefore, it does not measure the absorption cross section and might not be appropriate for any quantitative analyses like oxidation state analyses applying a linear combination least squares fit. We also simulated the conventional Np M_5 edge XANES spectra by integrating a larger (17

eV) emission energy region across the RIXS maps (magenta rectangles in Figure 6). It is clear that this Np M_5 edge XANES spectrum (magenta line on the top of the RIXS maps) has one broad peak and does not show any fine structure like the HR XANES spectra (green and red lines on the top of the RIXS maps). Because of the asymmetric distribution of the intensity with respect to the maxima of the normal emission lines (green lines), the conventional XANES spectra are shifted to higher energy compared to the HR XANES spectra (top of the RIXS maps). Further details on the contributions of the core−hole lifetime and experimental broadening to the RIXS maps are given by Vitova et al.[12g]

U and Np $M_{4,5}$-Edge HR-XANES. The Np M_5 edge HR XANES spectra of the Np(U) precipitate (Np cp and U cp) and the Np^{IV}, Np^{V}, and Np^{VI} reference compounds are depicted in Figures 7a and 8a. The Np^{V} and Np^{VI} compounds generally contain an axial neptunium *trans* dioxo moiety (O=Np=O) with a typical short bond length of less than about

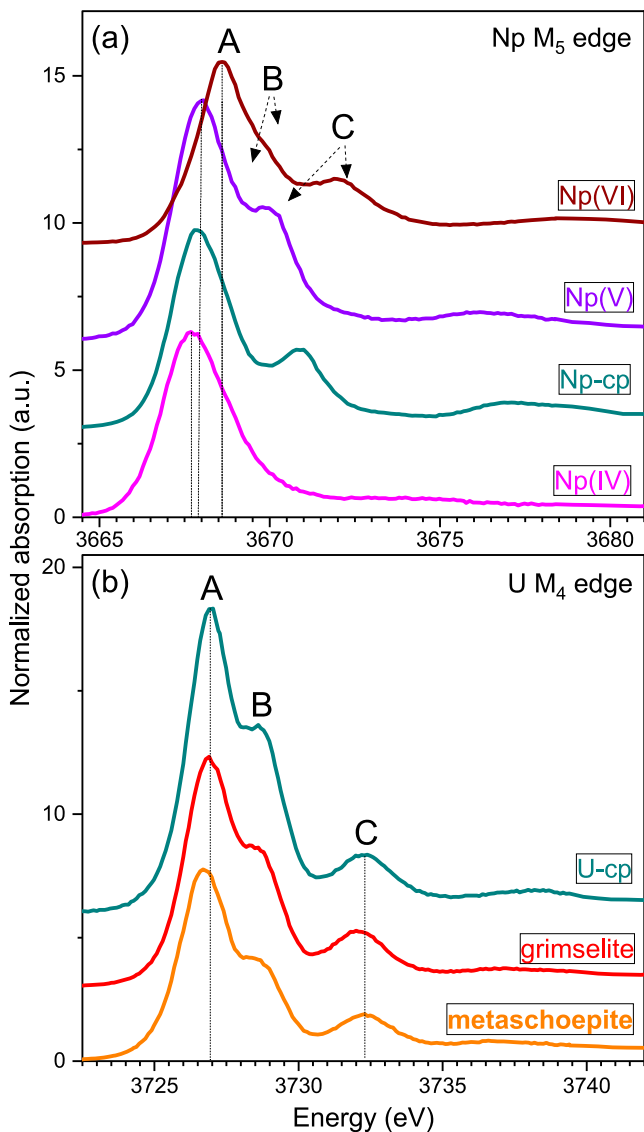**Figure 7.** (a) From top to bottom: Np M_5 edge HR XANES spectra of $Na_2Np^{VI}_2O_{7(cr)}$, $Ca_{0.5}Np^VO_2(OH)_2 \cdot 1.3H_2O_{(cr)}$, Np cp, and $Np^{IV}O_{2(am,hyd)}$. (b) U M_4 edge HR XANES spectra of U cp, grimselite $(K_3Na[UO_2(CO_3)_3] \cdot H_2O_{(cr)})$, and metaschoepite $([(UO_2)_4O (OH)_6] \cdot 5H_2O)$.

Figure 8. (a) From top to bottom: Np M_5 edge HR XANES spectra of $Na_2Np^{VI}_2O_{7(cr)}$, $Ca_{0.5}Np^VO_2(OH)_2 \cdot 1.3H_2O_{(cr)}$, Np cp, and $Np^{IV}O_{2(am,hyd)}$. (b) U M_4 edge HR XANES spectra of U cp, grimselite $(K_3Na[UO_2(CO_3)_3] \cdot H_2O_{(cr)})$, and metaschoepite $([(UO_2)_4O (OH)_6] \cdot 5H_2O)$.

1.80 Å (neptunyl). The elongated bond is referred to as neptunate. The energy position of the main absorption peak (A) of the Np M_5 edge HR XANES spectra shifts +0.3 ± 0.05 eV from Np^{IV} to Np^V and +0.6 eV ± 0.05 eV from Np^V to Np^{VI} (Table 3). The small +0.3 ± 0.05 eV energy shift between Np^{IV} and Np^V is not unusual because Np^V yl forms a covalent bond with the two axial O atoms, and as a result, there is shift of the electronic density toward Np^V, leading to an energy shift of the absorption edge of the spectrum to lower energies. For example, for Np L_3 edge XANES, the order is reversed: the spectrum of Np^V yl is at lower energy compared to Np^{IV}.[39]

The oxidation state of Np in Np(U) does not change from the initial 5+, as evidenced by the position of peak A at 3667.9 eV, which is only 0.1 eV lower than that for the Np^V reference spectrum. Similar minor energy shifts of the main peak are found for U M_4 edge HR XANES spectra for a series of U^{VI} materials and explained by different electronic densities on the
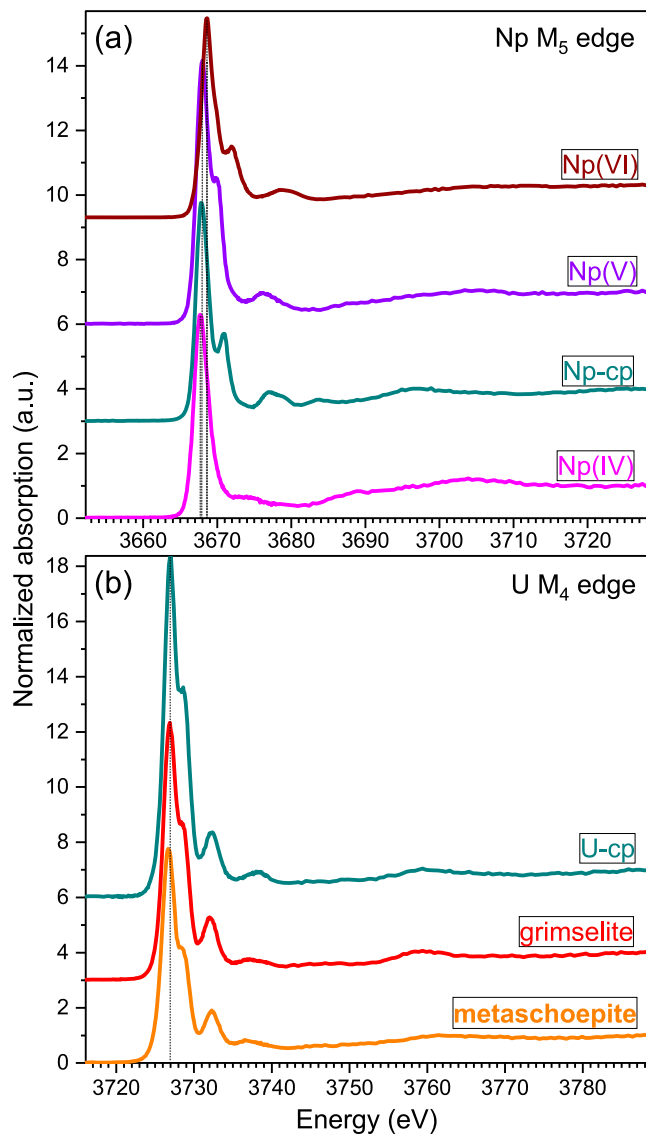
U^{VI} atom depending on its short and long range atomic environments.[40]

Peak C located at higher energies is well resolved in the Np M_5 edge HR XANES spectra of the Np^{VI} and Np^V reference compounds and the Np(U) solid. Peak B, present in the U M_4 edge HR XANES spectra of uranyl(VI) (Figure 7b), is visible only in the spectrum of Np^{VI} (Figure 7a) and overlaps with the main peak in the Np^V spectra. We attribute peaks B and C to electronic transitions to π^* and σ^* molecular orbitals with predominant contributions of the Np 5f and O 2p atomic orbitals in analogy to those for U^{VI} yl resolved in U M_4 edge HR XANES spectra.[12f] Peak A describes transitions to δ and φ largely nonbonding U 5f orbitals (cf. the simplified molecular orbital scheme for neptunyl in Figure 9). The molecular orbital schemes of uranyl and neptunyl in the ground state calculated with density functional theory (DFT), taking into account also spin−orbit coupling, are discussed by Vitova et al.[12f] We recently also compared ground state FDMNES calculations

Table 3. Energy Positions of the Spectral Peaks and Energy Differences for the Np/U M$_5$/M$_4$ Edge HR XANES Spectra of Np^{VI}, Np^V, Np cp, Np^{IV}, U cp, Grimselite (AMCSD 0005731), and Metaschoepite (AMCSD 0004319) Depicted in Figure 7^a

sample	A (eV)	B (eV)	C (eV)	B A (eV)	C A (eV)	R(An O$_{ax}$) (Å), ±0.01
Np^{VI} (Na$_2$Np$_2$O$_{7(cr)}$)	3668.6		3671.9		3.3	1.76^b
Np^V [Ca$_{0.5}$NpO$_2$(OH)$_2$ 1.3H$_2$O$_{(s)}$]	3668.0		3669.9		1.9	1.89^c
Np-cp [Np in the Np(U) precipitate]	3667.9		3670.9		3.0	1.83
Np^{IV} (NpO$_{2(am,hyd)}$)	3667.7					
U-cp [U in the Np(U) precipitate]	3726.9	3728.6	3732.3	1.7	5.4	1.78
grimselite (K$_3$Na[UO$_2$(CO$_3$)$_3$] H$_2$O)	3726.9	3728.6	3732.1	1.7	5.2	1.80
metaschoepite ([(UO$_2$)$_4$O(OH)$_6$] 5H$_2$O)	3726.7	3728.5	3732.3	1.8	5.6	1.77

^{a}The uncertainty of the energy positions is ±0.05 eV. The R(An=O) bond lengths are found from EXAFS (cf. Table 1). ^{b}Gaona et al.[38] ^{c}Fellhauer.[45]
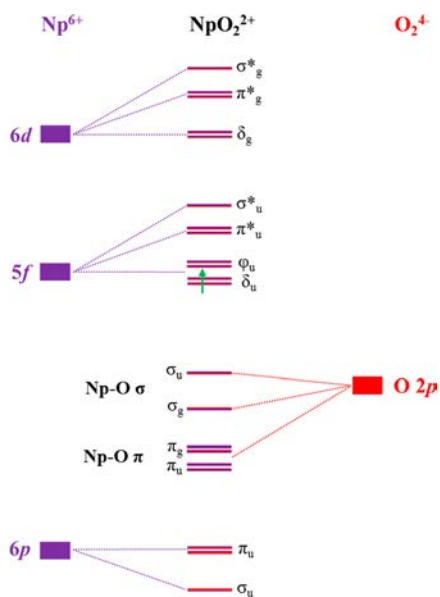

Figure 9. Qualitative molecular orbital scheme of neptunyl adapted from ref 49. Only frontier electrons are indicated.

with multiplet calculations of Pu M$_5$ edge HR XANES spectra of Pu^{VI} in aqueous solution (plutonyl) and found that the computed spectra are very similar. The multiplet effects and the experimental broadening lead to broadening of the peaks, but the σ* peak is well separated from the main absorption peak.[12e,g]

In order to compare the HR XANES spectra measured at the U M$_4$ and Np M$_5$ absorption edges and to verify that the assignments of the spectral peaks to electronic transitions to specific molecular orbitals of neptunyl are correct, we performed quantum chemical calculations of U M$_{4,5}$ and Np M$_5$ edge HR XANES and f DOS spectra with the FDMNES code (Figures 10−12). The computed U M$_4$ and M$_5$ edge HR XANES and f DOS spectra of grimselite are depicted in Figure 10. Because of selection rules (ΔJ = 0, ±1), 3d$_{3/2}$ → 5f$_{5/2}$ (M$_4$ edge), 3d$_{5/2}$ → 5f$_{5/2}$, and 3d$_{5/2}$ → 5f$_{7/2}$ (M$_5$ edge) electronic transitions take place at the two absorption edges. In addition, the screening of the core−hole differs (multiplet effects), which also has an influence on the spectra. The main differences between the calculated U M$_4$ and M$_5$ edge HR XANES spectra depicted in Figure 10 are the overlap of the first two peaks and the higher intensity of the second peak (transitions to π*) in the M$_4$ edge HR XANES spectrum (Figure 10a). The well separated peak C, describing transitions
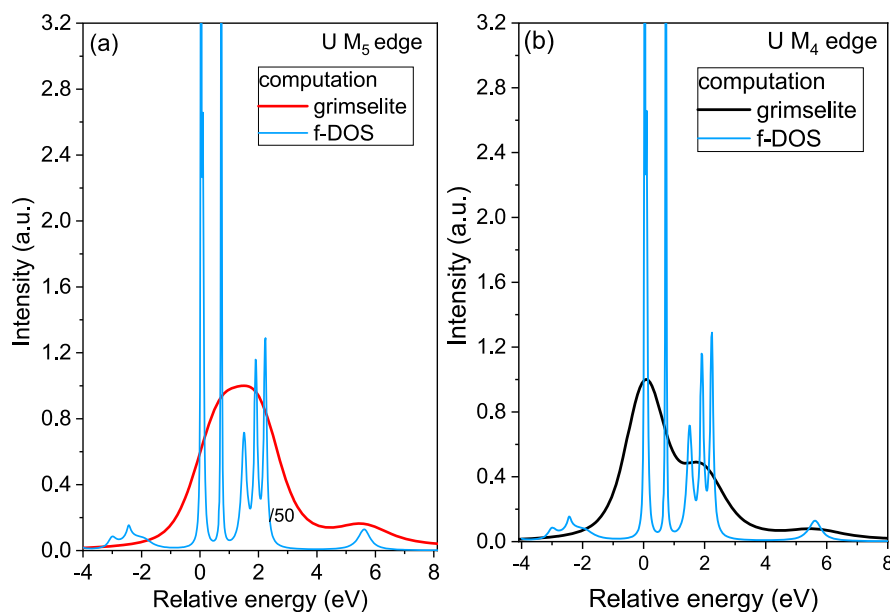

Figure 10. (a) U M$_5$ and (b) M$_4$ edge HR XANES and f DOS spectra of grimselite (K$_3$Na[UO$_2$(CO$_3$)$_3$]·H$_2$O$_{(cr)}$) computed with the FDMNES code. /50 means that the calculated intensity is reduced by a factor of 50 for a better comparison.
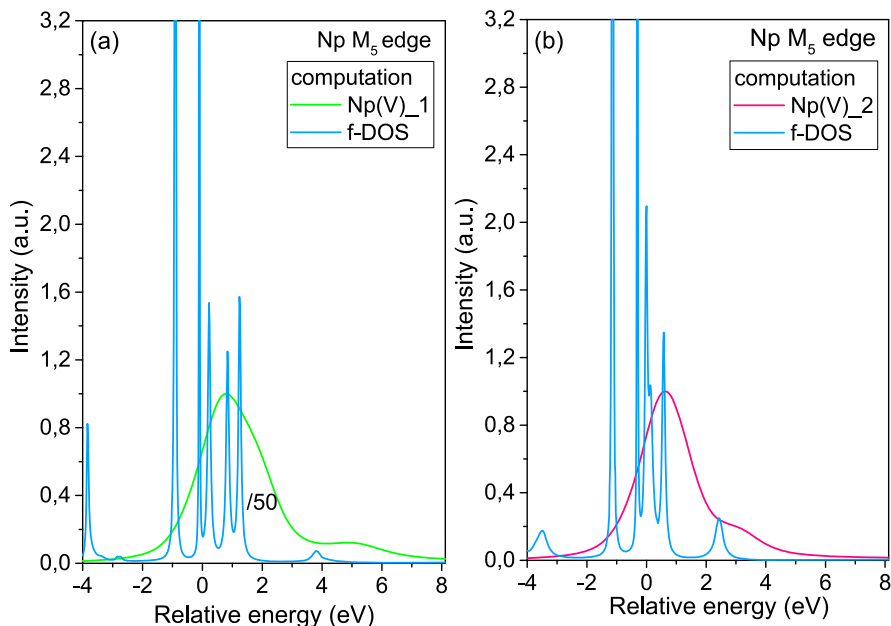
Figure 11. Np M_5 edge HR XANES and f DOS spectra of (a) $K_3[NpO_2(CO_3)_2]\cdot nH_2O(cr)$ (Np(V) 1) and (b) $K[NpO_2CO_3](cr)$ (Np(V) 2) computed with the FDMNES code. /50 means that the calculated intensity is reduced by a factor of 50 for a better comparison.
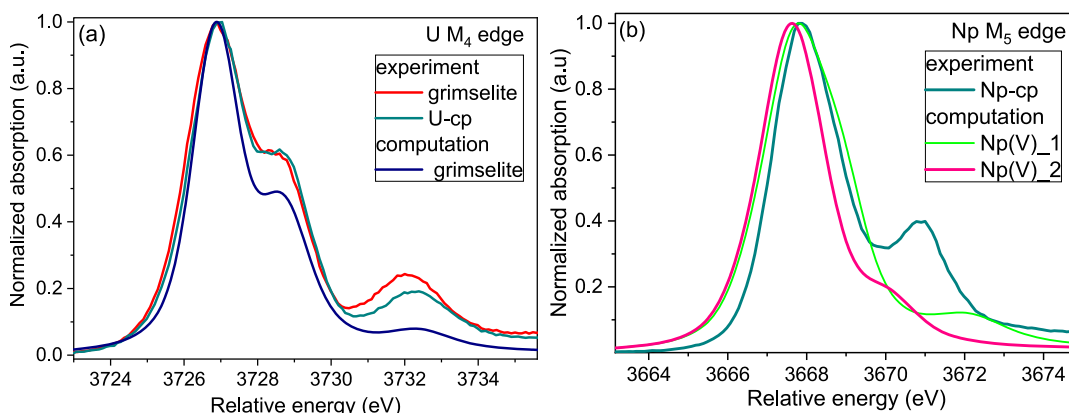

Figure 12. (a) U M_4 edge HR XANES spectra of grimselite ($K_3Na[UO_2(CO_3)_3]\cdot H_2O_{(cr)}$) and U cp and a computed spectrum of grimselite. (b) Np M_5 edge HR XANES spectrum of Np cp and computed spectra of $K_3[NpO_2(CO_3)_2]\cdot nH_2O(cr)$ and $K[NpO_2CO_3](cr)$. The computations were performed with the FDMNES code.

to the σ^* orbital, is at the same energy position in both spectra. The postedge regions of the two spectra are identical (cf. Figure S9). Considering these results, we conclude that the assignments of the spectral peaks for the Np M_5 edge HR XANES spectrum of neptunyl are appropriate.

The computed Np M_5 edge HR XANES and f DOS spectra of the two Np^V compounds ($K_3[NpO_2(CO_3)_2]\cdot nH_2O_{(cr)}$, Np(V) 1 and $K[NpO_2CO_3]_{(cr)}$, Np(V) 2) are shown in Figure 11a,b. Similar to the uranyl case, there is a peak in the Np f DOS and HR XANES spectra corresponding to the σ^* orbital (Np(V) 1 at 5 eV; Np(V) 2, at 3 eV). The U M_4 and Np M_5 edge computed spectra are compared to the experimental spectra in Figure 12. The calculated and experimental spectra of grimselite and U cp are in agreement (cf. Figures 12a and S10). The Np(U) sample is a mixture of the two Np^V compounds, which is also suggested by the energy position of peak C of the experimental Np cp spectrum located between the C peaks of the computed spectra of the two Np^V reference compounds. Note that the main absorption maxima of the calculated and experimental spectra are aligned.

The position of peak C varies significantly in all spectra (Table 3). In previous studies, it was shown that the energy shift between peaks A and C (ΔE_{C-A}) in the U^{VI} yl M_4 HR XANES spectra increases by shortening of the axial U−O bond length (Table 2 and Figure 7b).[40−42] DFT+U calculations of f DOS of uranyl(VI) suggest that changes of the equatorial U−O bond length do not directly influence ΔE_{C-A}. The computations were performed by fixing the axial U−O bond length and changing the equatorial U−O bond length.[41] However, there is an indirect influence because usually changes of the equatorial bond distances also lead to changes of the axial bond distances. There is often an inverse relationship: a shorter U−O_{eq} bond length leads to a longer U−O_{ax} bond length. DFT+U calculations also indicate that extreme bending of uranyl can lead to smaller ΔE_{C-A}, such as, for example, bending of the mostly linear O=U=O bond from 180° to 168.5°.[41] Note that materials with that strong bending of uranyl are very rare and are specifically synthesized.[43]

The correlation between ΔE_{C-A} and the axial U−O bond length is also valid for the Np M_5 edge HR XANES spectra of neptunyl; i.e., a larger ΔE_{C-A} value corresponds to a shorter axial Np−O bond (Table 2 and Figure 13). For example, Np^{VI}
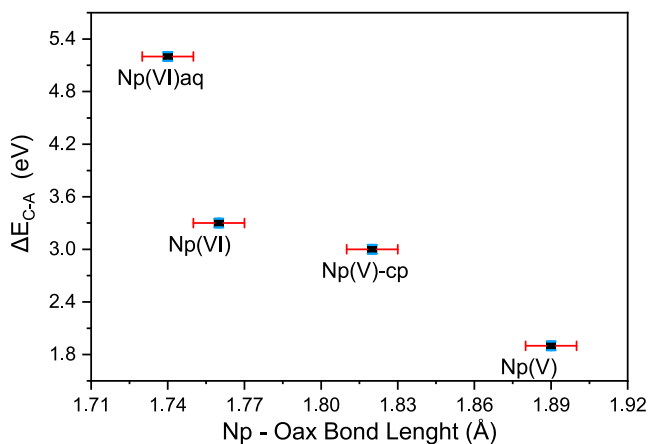

Figure 13. Energy shift between peaks A and C of the Np M_5 edge HR XANES spectra of neptunyl(V/VI) compounds (cf. Figure 7a) as a function of the Np−O axial bond length (cf. Table 3): Np(VI)aq in perchloric acid;[12g] Np(VI) in $Na_2Np^{VI}_2O_{7(cr)}$; Np(V) cp; Np(V) in $Ca_{0.5}Np^VO_2(OH)_2 \cdot 1.3H_2O_{(cr)}$.

in perchloric acid $[R(Np\!=\!O) = 1.74 \text{ Å}]^{44}$ has a larger ΔE_{C-A} = 5.2 eV^{12g} compared to that of $Na_2Np_2O_{7(cr)}$ with $R(Np\!=\!O)$ = 1.76 Å,[38] ΔE_{C-A} = 3.3 eV. There is a good agreement between the ΔE_{C-A} values and $R(Np-O_{ax})$ for Np cp and the Np^V reference; a smaller ΔE_{C-A} = 1.9 eV corresponds to a longer $R(Np\!=\!O) = 1.89(1)$ Å[45] for Np^V compared to that of ΔE_{C-A} = 3.0 eV, $R(Np\!=\!O) = 1.83(1)$ Å for Np cp (Table 3). Note also that the ΔE_{C-A} correlation with the bond length depends on the oxidation state of the actinyl but also on the coordination environment. Therefore, this analysis is most reasonable for actinyl materials with either the same An oxidation state or a similar atomic environment and different oxidation states.

No intense higher energy features are observed for the $Np(IV)O_{2(am,hyd)}$ spectrum, which is the case also for the U/Pu $M_{4,5}$ edge HR XANES spectra of U^{IV} and Pu^{IV} in UO_2 and PuO_2, respectively.[12d,46] In NpO_2, the Np ion has a $5f^3$ electronic configuration and cubic structure ($Fm3m$ symmetry) and, therefore, a different electronic structure compared to the Np^V ($5f^2$) and Np^{VI} ($5f^1$) reference compounds.

The U M_4 edge HR XANES spectrum reveals that the oxidation state of U in U cp is VI+ because of its very similar energy position compared to those in the spectra of the grimselite and metaschoepite references (Figure 7b). The 0.1 ± 0.05 eV energy shift between peaks A of the U M_4 edge HR XANES spectra for grimselite/U cp and metaschoepite can be attributed to a higher electronic density on the U atoms in metaschoepite. A ~0.2 eV smaller ΔE_{C-A} value is found for grimselite compared to U cp, in correlation with the slightly longer R $[+0.02$ Å; $R(U\!=\!O) = 1.80(1)$ Å].

DISCUSSION

We have applied the advanced spectroscopic U and Np $M_{4/5}$ edge HR XANES technique along with conventional characterization methods to describe the coordination structure and the U and Np oxidation states of Np^V coprecipitated with U^{VI} in a

potassium−sodium carbonate rich solution. The concentration of Np in the precipitate was much larger than that of U (<10% U + >90% Np), indicating lower solubility of the Np solid form at the given conditions (pH 10.5 and oxic conditions). The experimental and computational results as well as thermodynamic calculations reveal that neptunium(V) and uranium(VI) alkali metal carbonate solid phases are formed. The XRD, SEM−EDX, EXAFS, Np L_3 edge XANES, Raman, and Np M_5 edge HR XANES results demonstrate that $K[NpO_2CO_3]_{(cr)}$ and $K_3[NpO_2(CO_3)_2]\cdot nH_2O_{(cr)}$ are the Np phases formed. XRD reveals $K[NpO_2CO_3]_{(cr)}$, whereas EXAFS shows $K_3[NpO_2(CO_3)_2]\cdot nH_2O_{(cr)}$ as a predominant Np phase. This might be explained with higher structural disorder for the $K_3[NpO_2(CO_3)_2]\cdot nH_2O_{(cr)}$ phase. EXAFS probes the near atomic environment of U for all species, whereas XRD reveals only crystalline phases with long range atomic order.

One strong diffraction peak can be assigned to both the $K_3Na[(UO_2)(CO_3)_3]\cdot H_2O_{(cr)}$ and $UO_2CO_3\cdot H_2O_{(cr)}$ phases. Because of minor differences between the U L_3 edge EXAFS, U L_3 edge XANES, U M_4 edge HR XANES, and Raman spectra for the reference $K_3Na[(UO_2)(CO_3)_3]\cdot H_2O$ and the precipitated Np(U) compound, we conclude that the $K_3Na[(UO_2)(CO_3)_3]\cdot H_2O_{(cr)}$ phase dominates, whereas the $UO_2CO_3\cdot H_2O_{(cr)}$ phase might have a small contribution.

Additional implications regarding the possible Np^V incorporation into the U^{VI} phase could be derived from Raman spectroscopy because small variations in the frequencies of the Raman peaks can be characteristic for changes in the structure. Thus, $\nu_1(U\!=\!O)$ = 821 cm^{-1} is similar to that in pure grimselite $(K_3Na[(UO_2)(CO_3)_3]\cdot H_2O_{(cr)})$. Given that the $\nu_1(Np\!=\!O)$ stretch in the precipitate is also very close to that reported for neptunyl carbonates, the vibrational data corroborate two separate phases. However, the spectroscopic evidence does not allow one to completely rule out the incorporation of U into Np phases or Np into U phases.

Incorporation versus Precipitation. The formation of separate U and Np phases in this system warrants comment. Our initial assumption is that this is primarily due to the metastability of the system and the large difference of the solubilities of the potassium carbonate solid phases of Np and U (lower solubility for Np^V compared to that for U^{VI} for the given conditions). While there is precedent in the literature of An (in trace concentration) incorporation into the structure of uranyl minerals, we are specifically interested in what happens when high concentrations of U and Np are mixed. We note that the incorporation of Np into some uranyl phases occurs under mild hydrothermal approaches, as a direct substitution of either Np^V in a number of uranyl minerals, where a charge balancing substitution occurs,[47] or U^{VI} for Np^{VI} in metatorbernite $(Cu[(UO_2)_2(PO_4)_2]\cdot 8H_2O)_{(cr)}$,[48] while we have postulated that Am^{III} can be incorporated into the structure of grimselite.[35] The differing reactivities that we observe may be due to the distinct chemical behavior and crystal chemistry of the UO_2^{2+} and NpO_2^+ carbonates.

SUMMARY

In summary, we showed that neptunium carbonate phases with compositions close to $K[Np^VO_2CO_3]_{(cr)}$ and $K_3[Np^VO_2(CO_3)_2]\cdot nH_2O_{(cr)}$ coprecipitated from aqueous K−Na−U^{VI}−CO_3−H_2O systems along with the minor $K_3Na[(U^{VI}O_2)(CO_3)_3]_{(cr)}$ phase. A small contribution of $U^{VI}O_2CO_3\cdot H_2O_{(cr)}$ could not be excluded. We did not find clear evidence for the incorporation of U/Np in Np/U

crystalline/amorphous phases. Thermodynamic calculations suggested that $K_3Na[(UO_2)(CO_3)_3]_{(cr)}$ and $K_3[NpO_2(CO_3)_2]\cdot nH_2O_{(cr)}$ should be formed, so it might be that, in the short time scales of these experiments, the system did not reach thermodynamic equilibrium. However, given the uncertainties in the thermodynamic data available, the modeling results should not be overinterpreted. Np 3d4f RIXS and M_5 edge HR XANES were applied for the oxidation state and coordination studies of Np for the first time. The correlation between the size of the energy shift of peak C and that of peak A (ΔE_{C-A}) in Np M_5 edge HR XANES spectra and the axial Np−O bond lengths for neptunyl(V/VI) was demonstrated. The observation that neptunium(V) carbonates precipitate in preference to uranyl carbonates in alkaline K−Na−U^{VI}−CO$_3$−H$_2$O systems is important for understanding the fundamental chemical behavior of actinides in a potassium carbonate rich aqueous system.

AUTHOR INFORMATION

Corresponding Authors
*Email: tonya.vitova@kit.edu. Tel: +49 721 608 24024.
*Email: bakerrj@tcd.ie. Tel: +353 1 8963501.

ORCID
Tonya Vitova: 0000 0002 3117 7701
Tim Prüßmann: 0000 0002 7903 9199
Robert J. Baker: 0000 0003 1416 8659

Present Address
§V.M.: Department of Environmental Informatics, Helmholtz Centre for Environmental Research (UFZ), Permoserstrasse 15, 04318 Leipzig, Germany.

Author Contributions
The manuscript was written through contributions of all authors. All authors have given approval to the final version of the manuscript.

Notes
The authors declare no competing financial interest.

REFERENCES
(1) (a) Arai, Y.; Moran, P. B.; Honeyman, B. D.; Davis, J. A. In situ spectroscopic evidence for neptunium(V) carbonate inner sphere and outer sphere ternary surface complexes on hematite surfaces. *Environ. Sci. Technol.* **2007**, *41*, 3940−3944. (b) Clark, D. L.; Conradson, S. D.; Ekberg, S. A.; Hess, N. J.; Janecky, D. R.; Neu, M. P.; Palmer, P. D.; Tait, C. D. A multi method approach to actinide speciation applied to pentavalent neptunium carbonate complexation. *New J. Chem.* **1996**, *20*, 211−220. (c) Clark, D. L.; Conradson, S. D.; Ekberg, S. A.; Hess, N. J.; Neu, M. P.; Palmer, P. D.; Runde, W.; Tait, C. D. EXAFS studies of pentavalent neptunium carbonato complexes. Structural elucidation of the principal constituents of neptunium in groundwater environments. *J. Am. Chem. Soc.* **1996**, *118*, 2089−2090. (d) Madic, C.; Hobart, D. E.; Begun, G. M. Raman spectrometric studies of actinide(V) and (VI) complexes in aqueous sodium carbonate solution and of solid sodium actinide(V) carbonate compounds. *Inorg. Chem.* **1983**, *22*, 1494−1503. (e) Rai, D.; Hess, N. J.; Felmy, A. R.; Moore, D. A.; Yui, M. A Thermodynamic model for the solubility of NpO$_2$(am) in the aqueous K$^+$ HCO$_3^-$ CO$_3^{2-}$ OH H$_2$O system. *Radiochim. Acta* **1999**, *84*, 159−169.
(2) Ikeda Ohno, A.; Tsushima, S.; Takao, K.; Rossberg, A.; Funke, H.; Scheinost, A. C.; Bernhard, G.; Yaita, T.; Hennig, C. Neptunium carbonato complexes in aqueous solution: An electrochemical, spectroscopic, and quantum chemical study. *Inorg. Chem.* **2009**, *48*, 11779−11787.
(3) Balboni, E.; Morrison, J. M.; Wang, Z.; Engelhard, M. H.; Burns, P. C. Incorporation of Np(V) and U(VI) in carbonate and sulfate minerals crystallized from aqueous solution. *Geochim. Cosmochim. Acta* **2015**, *151*, 133−149.
(4) Heberling, F.; Denecke, M. A.; Bosbach, D. Neptunium(V) coprecipitation with calcite. *Environ. Sci. Technol.* **2008**, *42*, 471−476.
(5) (a) Smith, K. F.; Bryan, N. D.; Law, G. T. W.; Hibberd, R.; Shaw, S.; Livens, F. R.; Parry, S. A.; Mosselmans, J. F. W.; Morris, K. D. Np(V) sorption and solubility in high pH calcite systems. *Chem. Geol.* **2018**, *493*, 396−404. (b) Heberling, F.; Brendebach, B.; Bosbach, D. Neptunium(V) adsorption to calcite. *J. Contam. Hydrol.* **2008**, *102*, 246−252.
(6) (a) Nakata, K.; Nagasaki, S.; Tanaka, S.; Sakamoto, Y.; Tanaka, T.; Ogawa, H. Sorption and reduction of neptunium(V) on the surface of iron oxides. *Radiochim. Acta* **2002**, *90*, 665−669. (b) Nakata, K.; Nagasaki, S.; Tanaka, S.; Sakamoto, Y.; Tanaka, T.; Ogawa, H. Reduction rate of neptunium(V) in heterogeneous solution with magnetite. *Radiochim. Acta* **2004**, *92*, 145−149. (c) Moyes, L. N.; Jones, M. J.; Reed, W. A.; Livens, F. R.; Charnock, J. M.; Mosselmans, J. F. W.; Hennig, C.; Vaughan, D. J.; Pattrick, R. A. D. An X ray absorption spectroscopy study of neptunium(V) reactions with mackinawite (FeS). *Environ. Sci. Technol.* **2002**, *36*, 179−183. (d) Christiansen, B. C.; Geckeis, H.; Marquardt, C. M.; Bauer, A.; Römer, J.; Wiss, T.; Schild, D.; Stipp, S. L. S. Neptunyl (NpO$_2^+$) interaction with green rust, GR$_{Na,SO4}$. *Geochim. Cosmochim. Acta* **2011**, *75*, 1216−1226. (e) Fröhlich, D. R.; Amayri, S.; Drebert, J.; Grolimund, D.; Huth, J.; Kaplan, U.; Krause, J.; Reich, T. Speciation of Np(V) uptake by Opalinus Clay using synchrotron microbeam techniques. *Anal. Bioanal. Chem.* **2012**, *404*, 2151−2162. (f) Brookshaw, D. R.; Pattrick, R. A. D.; Bots, P.; Law, G. T. W.; Lloyd, J. R.; Mosselmans, J. F. W.; Vaughan, D. J.; Dardenne, K.; Morris, K. Redox Interactions of Tc(VII), U(VI), and Np(V) with Microbially Reduced Biotite and Chlorite. *Environ. Sci. Technol.* **2015**, *49*, 13139−13148. (g) Wylie, E. M.; Olive, D. T.; Powell, B. A. Effects of Titanium Doping in Titanomagnetite on Neptunium Sorption and Speciation. *Environ. Sci. Technol.* **2016**, *50*, 1853−1858.
(7) Scheinost, A. C.; Steudtner, R.; Hübner, R.; Weiss, S.; Bok, F. Neptunium^V Retention by Siderite under Anoxic Conditions: Precipitation of NpO$_2$−Like Nanoparticles and of Np^{IV} Pentacar bonate. *Environ. Sci. Technol.* **2016**, *50*, 10413−10420.
(8) (a) Burns, P. C.; Ewing, R. C.; Navrotsky, A. Nuclear fuel in a reactor accident. *Science* **2012**, *335*, 1184−1188. (b) Burakov, B. E.; Strykanova, E. E.; Anderson, E. B. Secondary uranium minerals on the

surface of Chernobyl "lava". *Mater. Res. Soc. Symp. Proc.* **1996**, *465*, 1309−1311.

(9) Burns, P. C.; Finch, R. J. Wyartite: Crystallographic evidence for the first pentavalent uranium mineral. *Am. Mineral.* **1999**, *84*, 1456−1460.

(10) Baker, R. J. Uranium minerals and their relevance to long term storage of nuclear fuels. *Coord. Chem. Rev.* **2014**, *266−267*, 123−136.

(11) Meredith, N. A.; Sigmon, G. E.; Simonetti, A.; Burns, P. C. Structural and Morphological Influences on Neptunium Incorporation in Uranyl Molybdates. *Cryst. Growth Des.* **2015**, *15*, 5293−5300.

(12) (a) Vitova, T.; Denecke, M. A.; Göttlicher, J.; Jorissen, K.; Kas, J. J.; Kvashnina, K.; Prüßmann, T.; Rehr, J. J.; Rothe, J. Actinide and lanthanide speciation with high energy resolution X ray techniques. *J. Phys.: Conf. Ser.* **2013**, *430*, 012117. (b) Kvashnina, K. O.; Butorin, S. M.; Martin, P.; Glatzel, P. Chemical State of Complex Uranium Oxides. *Phys. Rev. Lett.* **2013**, *111*, 253002. (c) Pidchenko, I.; Kvashnina, K. O.; Yokosawa, T.; Finck, N.; Bahl, S.; Schild, D.; Polly, R.; Bohnert, E.; Rossberg, A.; Göttlicher, J.; Dardenne, K.; Rothe, J.; Schäfer, T.; Geckeis, H.; Vitova, T. Uranium Redox Transformations after U(VI) Coprecipitation with Magnetite Nanoparticles. *Environ. Sci. Technol.* **2017**, *51*, 2217−2225. (d) Popa, K.; Prieur, D.; Manara, D.; Naji, M.; Vigier, J. F.; Martin, P. M.; Dieste Blanco, O.; Scheinost, A. C.; Prüßmann, T.; Vitova, T.; Raison, P. E.; Somers, J.; Konings, R. J. M. Further insights into the chemistry of the Bi U O system. *Dalton Trans* **2016**, *45*, 7847−7855. (e) Vitova, T.; Geckeis, H.; Bagus, P. S. Probing Actinide Covalency: Plutonium Electronic Structure Studies Using High Energy Resolution X Ray Spectroscopy. *Actinide Research Quarterly Second Quarter 2019, Pu Futures 2018 Conference 1*, 10−14, https://www.lanl.gov/discover/publications/actinide research quarterly/index.php. (f) Vitova, T.; Green, J. C.; Denning, R. G.; Loble, M.; Kvashnina, K.; Kas, J. J.; Jorissen, K.; Rehr, J. J.; Malcherek, T.; Denecke, M. A. Polarization dependent high energy resolution X ray absorption study of dicesium uranyl tetrachloride. *Inorg. Chem.* **2015**, *54*, 174−182. (g) Vitova, T.; Pidchenko, I.; Fellhauer, D.; Bagus, P. S.; Joly, Y.; Prüßmann, T.; Bahl, S.; González Robles, E.; Rothe, J.; Altmaier, M.; Denecke, M. A.; Geckeis, H. The role of the 5f valence orbitals of early actinides in chemical bonding. *Nat. Commun.* **2017**, *8*, 16053.

(13) Bahl, S.; Peuget, S.; Pidchenko, I.; Prüßmann, T.; Rothe, J.; Dardenne, K.; Delrieu, J.; Fellhauer, D.; Jégou, C.; Geckeis, H.; Vitova, T. Pu Coexists in Three Oxidation States in a Borosilicate Glass: Implications for Pu Solubility. *Inorg. Chem.* **2017**, *56*, 13982−13990.

(14) Li, Y.; Burns, P. C. The crystal structure of synthetic grimselite. *Can. Mineral.* **2001**, *39*, 1147−1151.

(15) Nipruk, O.; Knyazev, A.; Chernorukov, G.; Pykhova, Y. Synthesis and study of hydrated uranium(VI) oxides, $UO_3 \cdot nH_2O$. *Radiochemistry* **2011**, *53*, 146−150.

(16) Rothe, J.; Butorin, S.; Dardenne, K.; Denecke, M. A.; Kienzler, B.; Löble, M.; Metz, V.; Seibert, A.; Steppert, M.; Vitova, T.; Walther, C.; Geckeis, H. The INE Beamline for actinide science at ANKA. *Rev. Sci. Instrum.* **2012**, *83*, 043105.

(17) (a) Zimina, A.; Dardenne, K.; Denecke, M. A.; Doronkin, D. E.; Huttel, E.; Lichtenberg, H.; Mangold, S.; Prüßmann, T.; Rothe, J.; Spangenberg, T.; Steininger, R.; Vitova, T.; Geckeis, H.; Grunwaldt, J. D. CAT ACT A new highly versatile x ray spectroscopy beamline for catalysis and radionuclide science at the KIT synchrotron light facility ANKA. *Rev. Sci. Instrum.* **2017**, *88*, 113113. (b) Kleymenov, E.; et al. Five element Johann type X ray emission spectrometer with a single photon counting pixel detector. *Rev. Sci. Instrum.* **2011**, *82*, 065107.

(18) (a) Walshe, A.; Prüßmann, T.; Vitova, T.; Baker, R. J. An EXAFS and HR XANES study of the uranyl peroxides $[UO_2(\eta^2 O_2)(H_2O)_2] \cdot nH_2O$ (n = 0, 2) and uranyl (oxy)hydroxide $[(UO_2)_4O(OH)_6] \cdot 6H_2O$. *Dalton Trans.* **2014**, *43*, 4400−4407. (b) Glatzel, P.; Bergmann, U. High resolution 1s core hole X ray spectroscopy in 3d transition metal complexes electronic and structural information. *Coord. Chem. Rev.* **2005**, *249*, 65−95.

(19) Solé, V. A.; Papillon, E.; Cotte, M.; Walter, Ph.; Susini, J. A multiplatform code for the analysis of energy dispersive X ray fluorescence spectra. *Spectrochim. Acta, Part B* **2007**, *62*, 63−68.

(20) Ravel, B.; Newville, M. ATHENA, ARTEMIS, HEPHAESTUS: data analysis for X ray absorption spectroscopy using IFEFFIT. *J. Synchrotron Radiat.* **2005**, *12*, 537−541.

(21) Volkov, Y. F.; Visyashcheva, G. I.; Tomilin, S. V.; Kapshukov, I. I.; Rykov, A. G. Determination of the crystal structure of $M_3AnO_2(CO_3)_2 \cdot nH_2O$. *Radiokhimiya* **1981**, *23*, 243−247.

(22) Rehr, J. J.; Kas, J. J.; Vila, F. D.; Prange, M. P.; Jorissen, K. Parameter free calculations of X ray spectra with FEFF9. *Phys. Chem. Chem. Phys.* **2010**, *12*, 5503−5513.

(23) (a) Vitova, T.; Kvashnina, K. O.; Nocton, G.; Sukharina, G.; Denecke, M. A.; Butorin, S. M.; Mazzanti, M.; Caciuffo, R.; Soldatov, A.; Behrends, T.; Geckeis, H. High energy resolution x ray absorption spectroscopy study of uranium in varying valence states. *Phys. Rev. B: Condens. Matter Mater. Phys.* **2010**, *82*, 235118. (b) Bunau, O.; Joly, Y. Self consistent aspects of X ray absorption calculations. *J. Phys.: Condens. Matter* **2009**, *21*, 345501.

(24) Keenan, T. K.; Kruse, F. H. Potassium Double Carbonates of Pentavalent Neptunium, Plutonium, and Americium. *Inorg. Chem.* **1964**, *3*, 1231−1232.

(25) Parkhurst, D. L.; Appelo, C. A. J. Description of input and examples for PHREEQC version 3—a computer program for speciation, batch reaction, one dimensional transport, and inverse geochemical calculations. *US geological survey techniques and methods* **2013**, *6*, 497.

(26) Grivé, M.; Duro, L.; Colàs, E.; Giffaut, E. Thermodynamic data selection applied to radionuclides and chemotoxic elements: An overview of the ThermoChimie TDB. *Appl. Geochem.* **2015**, *55*, 85−94.

(27) *Update on the chemical thermodynamics of uranium, neptunium, plutonium, americium and technetium*; Guillaumont, R., Mompean, F. J., Eds.; Elsevier: Amsterdam, The Netherlands, 2003.

(28) Kaszuba, J. P.; Runde, W. H. The aqueous geochemistry of neptunium: Dynamic control of soluble concentrations with applications to nuclear waste disposal. *Environ. Sci. Technol.* **1999**, *33*, 4427−4433.

(29) Novak, C. F.; Mahamid, I. A.; Becraft, K. A.; Carpenter, S. A.; Hakem, N.; Prussin, T. Measurement and thermodynamic modeling of Np(V) solubility in aqueous K_2CO_3 solutions to high concentrations. *J. Solution Chem.* **1997**, *26*, 681−697.

(30) Fanghänel, Th.; Neck, V.; Kim, J. I. Thermodynamics of neptunium(V) in concentrated salt solutions: II. Ion interaction (Pitzer) parameters for Np(V) hydrolysis species and carbonate complexes. *Radiochim. Acta* **1995**, *69*, 169.

(31) Neck, V.; Runde, W.; Kim, J. I. Solid liquid equilibria of neptunium(V) in carbonate solutions of different ionic strengths II. Stability of the solid phases. *J. Alloys Compd.* **1995**, *225*, 295−302.

(32) (a) Keenan, T. K.; Kruse, F. H. Potassium double carbonates of pentavalent neptunium, plutonium, and americium. *Inorg. Chem.* **1964**, *3*, 1231−1232. (b) Visyashcheva, G. I.; Volkov, Y. F.; Simakin, G. A.; Kapshukov, I. I.; Bevz, A. S.; Yakovlev, G. N. Composition and some properties of solid carbonates of pentavalent neptunium with potassium obtained from K_2CO_3 solutions. *Radiokhimiya* **1974**, *16*, 853−859.

(33) (a) Volkov, Y. F.; Kapshukov, I. I.; Visyashcheva, G. I.; Yakovlev, G. N. X ray investigation of neptunium (V), plutonium (V), and americium (V) monocarbonates with potassium. *Radiokhimiya* **1974**, *16*, 863−867. (b) Volkov, Y. F.; Tomilin, S. V.; Visyashcheva, G. I.; Kapshukov, I. I. X ray structure analysis of $LiNpO_2CO_3$ and $NaNpO_2CO_3$. *Radiokhimiya* **1979**, *21*, 668−672. (c) Volkov, Y. F.; Visyashcheva, G. I.; Kapshukov, I. I. Production and identification of hydrate forms of sodium monocarbonatoneptunaylate. *Radiokhimiya* **1977**, *19*, 319−323. (d) Volkov, Y. F.; Visyashcheva, G. I.; Kapshukov, I. I.; Simakin, G. A.; Yakovlev, G. N. Composition and properties of carbonates of the pentavalent actinides. *Radiokhimiya* **1976**, *18*, 96−100.

(34) Finch, R. J.; Cooper, M. A.; Hawthorne, F. C.; Ewing, R. C. Refinement of the crystal structure of rutherfordine. *Can. Mineral.* **1999**, *37*, 929–938.

(35) Biswas, S.; Steudtner, R.; Schmidt, M.; McKenna, C.; Leon Vintro, L.; Twamley, B.; Baker, R. J. An investigation of the interactions of Eu^{3+} and Am^{3+} with uranyl minerals: implications for the storage of spent nuclear fuel. *Dalton Trans* **2016**, *45*, 6383–6393.

(36) Vochten, R.; Deliens, M. Blatonite, $UO_2CO_3 \cdot H_2O$, a new uranyl carbonate monohydrate from San Juan County, Utah. *Can. Mineral.* **1998**, *36*, 1077–1081.

(37) (a) Fellhauer, D.; Neck, V.; Altmaier, M.; Lützenkirchen, J.; Fanghänel, T. Solubility of tetravalent actinides in alkaline $CaCl_2$ solutions and formation of $Ca_4[An(OH)_8]^{4+}$ complexes: A study of Np(IV) and Pu(IV) under reducing conditions and the systematic trend in the An(IV) series. *Radiochim. Acta* **2010**, *98*, 541–548. (b) Fellhauer, D.; Rothe, J.; Altmaier, M.; Neck, V.; Runke, J.; Wiss, T.; Fanghänel, T. Np (V) solubility, speciation and solid phase formation in alkaline $CaCl_2$ solutions. Part I: Experimental results. *Radiochim. Acta* **2016**, *104*, 355–379. (c) Gaona, X.; Fellhauer, D.; Altmaier, M. Thermodynamic description of Np(VI) solubility, hydrolysis, and redox behavior in dilute to concentrated alkaline NaCl solutions. *Pure Appl. Chem.* **2013**, *85*, 2027–2049.

(38) Gaona, X.; Fellhauer, D.; Rothe, J.; Altmaier, M. Investigations on Np(VI) in alkaline NaCl solutions: aqueous chemistry and solid phase characterization. In *4th Annual Workshop Proceedings of the Collaborative Project "Redox Phenomena Controlling Systems" (7th EC FP CP RECOSY)*; Altmaier, M., Kienzler, B., Duro, L., Grivé, M., Montoya, V., Eds.; (KIT Scientific Reports; 7626), KIT Scientific Publishing: Karlsruhe, Germany, 2012; pp 343–352; ISBN: 978 3 86644 921 3.

(39) Gaona, X.; Tits, J.; Dardenne, K.; Liu, X.; Rothe, J.; Denecke, M. A.; Wieland, E.; Altmaier, M. Spectroscopic investigations of Np(V/VI) redox speciation in hyperalkaline TMA (OH, Cl) solution. *Radiochim. Acta* **2012**, *100*, 759–770.

(40) Podkovyrina, Y; Pidchenko, I; Prußmann, T; Bahl, S; Gottlicher, J.; Soldatov, A; Vitova, T Probing covalency in the UO3 polymorphs by U M4 edge. *J. Phys.: Conf. Ser.* **2016**, *712*, 012092.

(41) Vitova, T.; Pidchenko, I.; Biswas, S.; Beridze, G.; Dunne, P. W.; Schild, D.; Wang, Z.; Kowalski, P. M.; Baker, R. J. Dehydration of the Uranyl Peroxide Studtite, $[UO_2(\eta^2 O_2)(H_2O)_2] \cdot 2H_2O$, Affords a Drastic Change in the Electronic Structure: A Combined X ray Spectroscopic and Theoretical Analysis. *Inorg. Chem.* **2018**, *57*, 1735–1743.

(42) (a) Zegke, M.; Zhang, X.; Pidchenko, I.; Hlina, J. A.; Lord, R. M.; Purkis, J.; Nichol, G. S.; Magnani, N.; Schreckenbach, G.; Vitova, T.; Love, J. B.; Arnold, P. L. *Chem. Sci.* **2019**, *10*, 9740–9751. (b) Hunault, M. O. J. Y.; Lelong, G.; Cormier, L.; Galoisy, L.; Solari, P. L.; Calas, G. Speciation Change of Uranyl in Lithium Borate Glasses. *Inorg. Chem.* **2019**, *58*, 6858–6865.

(43) Hayton, T. W. Understanding the origins of $O_{yl}-U-O_{yl}$ bending in the uranyl (UO_2^{2+}) ion. *Dalton Trans.* **2018**, *47*, 1003–1009.

(44) Grigor'ev, M. S.; Krot, N. N. Synthesis and single crystal X ray diffraction study of U(VI), Np(VI), and Pu(VI) perchlorate hydrates. *Radiochemistry* **2010**, *52*, 375–381.

(45) Fellhauer, D. Untersuchungen zur Redoxchemie und Löslichkeit von Neptonium und Plutonium. Ph.D. Thesis, University of Heidelberg, Heidelberg, Germany, 2013.

(46) Vitova, T.; Pidchenko, I.; Fellhauer, D.; Prüßmann, T.; Bahl, S.; Dardenne, K.; Yokosawa, T.; Schimmelpfennig, B.; Altmaier, M.; Denecke, M.; Rothe, J.; Geckeis, H. Exploring the electronic structure and speciation of aqueous and colloidal Pu with high energy resolution XANES and computations. *Chem. Commun.* **2018**, *54*, 12824–12827.

(47) Burns, P. C.; Klingensmith, A. L. Uranium mineralogy and neptunium mobility. *Elements* **2006**, *2*, 351–356.

(48) Meredith, N. A.; Polinski, M. J.; Cross, J. N.; Villa, E. M.; Simonetti, A.; Albrecht Schmitt, T. E. Synthetic Influences on Neptunium Incorporation in Naturally Occurring Copper Uranyl Phosphates. *Cryst. Growth Des.* **2013**, *13*, 386–392.

(49) Hay, P. J.; Martin, R. L.; Schreckenbach, G. Theoretical studies of the properties and solution chemistry of AnO_2^{2+} and AnO_2^+ aquo complexes for An = U, Np, and Pu. *J. Phys. Chem. A* **2000**, *104*, 6259–6270. (b) Clark, D. L.; Hecker, S. S.; Jarvinen, G. D.; Neu, M. P. In *The Chemistry of the Actinide and Transactinide Elements*; Morss, L. R., et al., Eds.; Springer, 2006; pp 813–1264